









Assessing the Optimal Tsunami Inundation Modeling Strategy for Large Earthquakes in Subduction Zones

A. Scala^{1,2} , S. Lorito² , C. Escalante Sánchez³, F. Romano² , G. Festa^{1,2} , A. Abbate^{2,4} ,
H. B. Bayraktar² , M. J. Castro³, J. Macías³ , and J. M. Gonzalez-Vida³ 

¹Department of Physics “Ettore Pancini”, University Federico II, Napoli, Italy, ²Istituto Nazionale di Geofisica e Vulcanologia, Rome, Italy, ³EDANYA Group, University of Malaga, Malaga, Spain, ⁴Department of Mathematics, Informatics and Geosciences, University of Trieste, Trieste, Italy

Key Points:

- Slow and large ruptures (e.g., tsunami earthquakes and megathrust) require a time-dependent, non-hydrostatic modeling
- Deeper, high stress-drop earthquakes might be modeled through an instantaneous source, shallow water approximation
- Inundation depends on bathymetric features: larger inundations on steeper depth gradients and resonant runup amplifications are observed

Supporting Information:

Supporting Information may be found in the online version of this article.

Correspondence to:

A. Scala,
antonio.scala@unina.it

Citation:

Scala, A., Lorito, S., Escalante Sánchez, C., Romano, F., Festa, G., Abbate, A., et al. (2024). Assessing the optimal tsunami inundation modeling strategy for large earthquakes in subduction zones. *Journal of Geophysical Research: Oceans*, 129, e2024JC020941. <https://doi.org/10.1029/2024JC020941>

Received 18 JAN 2024

Accepted 6 AUG 2024

Author Contributions:

Conceptualization: A. Scala, S. Lorito, G. Festa, M. J. Castro

Data curation: A. Scala, F. Romano

Formal analysis: A. Scala, C. Escalante Sánchez, F. Romano, A. Abbate, H. B. Bayraktar

Investigation: A. Scala, S. Lorito, C. Escalante Sánchez, F. Romano, G. Festa, A. Abbate, H. B. Bayraktar

Methodology: A. Scala, S. Lorito, C. Escalante Sánchez, F. Romano, G. Festa, M. J. Castro, J. Macías,

J. M. Gonzalez-Vida

Software: A. Scala, C. Escalante Sánchez, M. J. Castro

© 2024. The Author(s).

This is an open access article under the terms of the [Creative Commons Attribution License](https://creativecommons.org/licenses/by/4.0/), which permits use, distribution and reproduction in any medium, provided the original work is properly cited.

Abstract Tsunamis are rare events involving several complex physical phenomena. Due to this complexity and the relative scarcity of observations, tsunami research makes extensive use of numerical simulations. For seismogenic tsunamis, the source is often modeled as an instantaneous sea-floor displacement (IS), while the tsunami propagation and inundation is computed through a shallow water approximation (SW). Here, we investigate what is the best tsunami inundation modeling strategy for different realistic earthquake source size and duration. We use 1D earthquake-tsunami coupled simulations of large $M > 8$ earthquakes in Tohoku-like subduction zone to test for which conditions the IS and/or the SW approximations can simulate with enough accuracy the tsunami evolution. We use as a reference a time-dependent (TD), multi-layer, non-hydrostatic (NH) 1D model. Source duration, and size, are based on 1D dynamic rupture simulations with realistic stress drop and rigidity. We show that slow ruptures, generating slip in the shallow part of subduction zones (e.g., tsunami earthquakes), and very large events, with an along-dip extent comparable with the trench-coast distance (as occurs for megathrust events) require a TD-NH modeling, especially for regions with steep coastal bathymetry. Conversely, deeper, higher stress-drop events can be modeled through an IS-SW approximation. We finally show that: (a) steeper bathymetries generate larger runups and, (b) a resonant mechanism emerges with runup amplifications associated with larger source size on flatter bathymetries. These results, obtained with 1D modeling, can serve as a guide for the appropriate 2/3D simulation approach for applications ranging from fundamental tsunami science to computational-intensive hazard assessments.

Plain Language Summary In the last two decades, tsunamis originated by large earthquakes have generated major damage and, according to the World Health Organization, more than 250 k casualties (more than 200 k due to the 2004 Indian Ocean tsunami). Strategies to quantify and mitigate the associated risk are based on numerical simulations of the physical processes regulating the generation, propagation of the waves and subsequent flooding on the coast. These simulations require significant computational resources. To make simulations more affordable, numerous approximations are introduced that need to be tested. In this work, we studied which earthquakes, depending on the speed at which they deform the sea bottom when they trigger a tsunami, and on how big they are, require a more detailed modeling approach, and which ones, instead, might be accurately simulated through approximated approaches. We also show how such findings are related to different bathymetric characteristics near the coast and inland, which may enhance or reduce the tsunami effects.

1. Introduction

Due to the rare occurrence of tsunamis and the strong influence of bathymetry and coastal morphology on tsunami evolution, the tsunami community makes use of numerical simulations to compensate for the scarcity of observations (see e.g., Babeyko et al., 2022; Behrens et al., 2021; Sugawara, 2021). Here, we consider tsunamis generated by earthquakes in subduction zones, since the most destructive tsunamis in the last decades were generated by inter-plate thrust subduction events (Davies & Griffin, 2020; Grezio et al., 2017). For these sources, tsunami simulations require the numerical modeling of the earthquake source process, the solid-fluid interaction during the tsunami generation, and the wave propagation on a complex bathymetry up to the inundation of the coastal topography. Numerical modeling of these diverse physical processes typically requires different solvers with a certain level of coupling between them. They range from the simplest solution consisting of seafloor displacement induced by instantaneous slip (Okada, 1985) to more complex modeling implementing either a two-

Supervision: A. Scala, S. Lorito, G. Festa, M. J. Castro, J. Macías, J. M. Gonzalez-Vida

Validation: A. Scala, S. Lorito, F. Romano, G. Festa

Visualization: S. Lorito

Writing – original draft: A. Scala, S. Lorito, C. Escalante Sánchez, F. Romano, G. Festa, M. J. Castro

Writing – review & editing: A. Scala, S. Lorito, C. Escalante Sánchez, F. Romano, G. Festa, A. Abbate, H. B. Bayraktar, M. J. Castro, J. Macías, J. M. Gonzalez-Vida

step (Krenz et al., 2021; Lotto & Dunham, 2015; Lotto et al., 2019; Madden et al., 2020; Saito et al., 2019) or a fully coupled approach to describe the seismic and the tsunami source processes (Abrahams et al., 2023).

The complexity of the physics considered generally results in an increase of the computational cost of the numerical solutions. For instance, to numerically model a past tsunami event, recorded by deep-sea sensors, it may be sufficient to use a linear propagation solver, leaving the available computational resources to the exploration of the source parameters and the related uncertainties. If the observable is instead the tsunami runup inland, a more costly nonlinear approach may be needed. This is particularly relevant when an application requires many high-resolution simulations, such as in probabilistic tsunami hazard analysis (PTHA, Basili et al., 2021; Behrens et al., 2021; Davies et al., 2018; Gibbons et al., 2020; Grezio et al., 2017), inverse problems (Romano et al., 2020, 2021), or tsunami forecasting for early warning purposes (Selva et al., 2021).

One way to cope with the containment of the computational cost is to approximate the tsunami initial sea level perturbation, its height after shoaling, or the runup process with analytical or stochastic methods (Abbate et al., 2024; Brocchini & Peregrine, 1996; Gailler et al., 2018; Glimsdal et al., 2019; Souty & Gailler, 2021). An emerging way to approach the problem is to exploit emulators as surrogates of the simulations (Ehara et al., 2023; Gopinathan et al., 2021) or AI-based techniques to estimate the inundation parameters from offshore or low-resolution simulations (Ehara et al., 2023; Makinoshima et al., 2021).

All these strategies are complementary to the purpose of this study, which aims to establish an optimal modeling strategy for the specific case of large earthquakes in subduction zones and the ensuing tsunamis, investigating a broad range of seismic source conditions, accounting for realistic conditions in terms of stress drop, fault extent and medium properties.

The subduction plate interface is often represented as a planar or a segmented interface (LeVeque et al., 2016; Li et al., 2016; Sepúlveda et al., 2017). However, recently, curved surfaces are being modeled increasingly often (Nakano et al., 2020; Scala et al., 2020; Tonini et al., 2020). The seismic rupture on the interface is modeled as an instantaneous elastic dislocation, or as the linear superposition of dislocations of different amplitude representing heterogeneous slip distributions, in a homogeneous half-space (Meade, 2007; Okada, 1985). The resulting instantaneous elastic deformation of the sea floor is eventually smoothed (Kajiura, 1963) to obtain a static sea surface anomaly, that generates waves owing to gravity. The tsunami propagation is then numerically computed in the nonlinear shallow water approximation (Stoker J. J., 1992) until the coastal inundation, fully neglecting dispersive wave effects.

However, the rupture process is not instantaneous. During this process, the zones affected by elastic dislocation change as the seismic rupture expands. The spatial and temporal scales of the seismic rupture process have a wide range of variability making the above-mentioned approximations valid only for specific applications (see Abrahams et al., 2023 and references therein). To the first order, we can characterize the tsunami source duration and size through the duration and extent of the initial sea level perturbation which, in turn, can be related to the average rigidity and the stress drop of the seismic source (Bilek & Lay, 1999; Geist & Bilek, 2001). The input to a shallow water model is often smoothed with a Kajiura filter to limit unphysical short wavelength components. For slow ruptures, or very short-wavelength sea bottom displacements, a more accurate modeling of the time-dependent coupling between the sea bottom and the water layer, and of the subsequent tsunami evolution may be necessary (see, as well, the discussion in Abrahams et al., 2023 and references therein). Beyond that, several numerical comparisons against experimental data (Ma et al., 2012; Macías et al., 2021a, 2021b) demonstrated that accounting for dispersive effects is essential for faithfully simulating waves in the vicinity of the continental shelf, as well as to model runup, shoaling, and wet-dry areas. For example, for outer-rise normal faulting, dispersion might amplify tsunami waves (Baba et al., 2021).

Here, we aim to address if and for which cases a modeling of time-dependent rupture complexity and non-hydrostatic regime accounting for a more physically realistic modeling of seismic source and tsunami processes, respectively, are necessary to guarantee the accuracy of the results for the simulation of tsunamis generated by large earthquakes in subduction zones. This approach might also offer a new strategy for addressing the trade-off between required accuracy and computational demand.

We initiate the simulations through a spatial 1D, time-dependent sea-level displacement (along the x -direction of the sketches in Figures 1 and 2a) generated by a 1D numerical model of the seismic rupture (Murphy et al., 2016, 2018; Scala et al., 2017, 2019). This displacement is the input for the 1D tsunami generation and evolution which

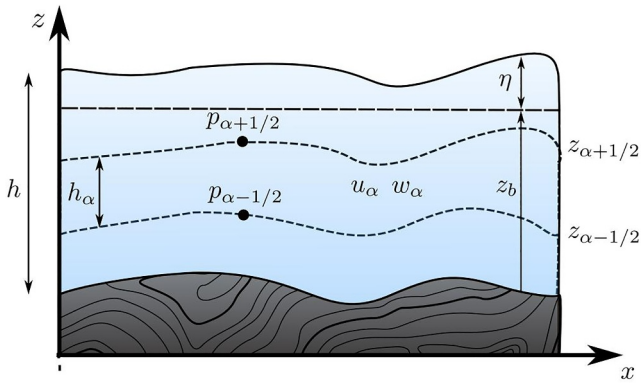


Figure 1. Schematic diagram describing the multilayer system.

is simulated through a non-hydrostatic 3-layer tsunami code (Escalante et al., 2019, 2023a). The bathymetry and topography adopted in this study are modeled through simplified 1-D versions of transects perpendicular to the coast of Tohoku in Japan to investigate general effects due to very steep, very flat and intermediate bathymetry slopes nearshore and on the coast. This setup is used as the “ground-truth” to benchmark more simplified approaches using either instantaneous seafloor displacement, or a one-layer shallow water scheme, or a combination of the two.

The use of a 1D approach presents some limitations. Indeed, it does not take into account the significant along-strike depth-dependent source propagation which characterizes both regular megathrust and tsunami earthquakes (Polet & Kanamori, 2000). Moreover, the 1D setup does not allow the modeling of the longshore tsunami processes, like local resonances and amplifications or edge waves (Geist, 2016; Kim et al., 2016; Koyano et al., 2021). Neverthe-

less, such a modeling approach allows us to perform a large number of simulations spanning a broad range of rupture velocities and extent on different bathymetric profiles and coastal slopes, and with enough spatial resolution to perform inundation modeling. The metrics used to validate the different approaches/approximations are the sea-surface evolution, the offshore maximum wave amplitude at different depths, seaward and landward from the trench, the flow depth and the maximum runup inland.

2. Methods: Coupling Modeling of Earthquake and Tsunami

2.1. Earthquake Rupture Dynamics Modeling

To model 1D earthquake rupture dynamics in a 2D elastic domain, we used the same approach proposed in Scala et al. (2017, 2019). We solve the general elastodynamic problem:

$$\begin{cases} \rho(x)\ddot{u}(x,t) = \nabla \cdot \sigma(x,t) \\ \sigma(x,t) = \mathbf{C}(x) : \nabla u(x,t) \end{cases} \quad (1)$$

In Equation 1, x is the position, t the time, $\rho(x)$ is the bulk density, $\sigma(x,t)$ and $\mathbf{C}(x)$ the stress and the elastic coefficient tensors respectively, while $u(x,t)$ represents the particle displacement. The traction $T = \sigma \cdot n$ is imposed to be zero on the seafloor interface, neglecting the acoustic coupling between the seafloor and the water itself.

The fault is modeled through a domain decomposition around a 1D interface where the continuity of the traction T is imposed. The fault slip and slip rate are defined as $\delta u(\hat{x},t) = u_2(x_2,t) - u_1(x_1,t)$ and $\delta v(\hat{x},t) = v_2(x_2,t) - v_1(x_1,t)$ respectively, with \hat{x} representing a generic point on the interface while the subscripts 1 and 2 mark the quantities computed on the two sides of the fault. The contact between the two sides of the fault is modeled through the Signorini's condition: the normal traction is either negative and hence the two lips are in contact and prone to frictionally slide or equal to zero, making each side of the interface a free surface and generating an opening (see also Equation 2 in Scala et al., 2019). When the two sides of the fault interface are in contact, the frictional sliding is governed by the following Coulomb condition:

$$\begin{cases} [T^t(\hat{x},t) - c(\hat{x}) + fT^n(\hat{x},t)] \cdot |\delta v^t(\hat{x},t)| = 0 \\ [T^n(\hat{x},t) - c(\hat{x}) + fT^t(\hat{x},t)] \leq 0 \end{cases} \quad (2)$$

In Equation 2, the superscripts t and n represent the tangential and normal directions with respect to the interface, c is a level of cohesion on the fault. The friction f is here assumed to linearly decrease with slip from a static level f_s to a dynamic one f_d over a finite length of slip D_c (slip weakening; Ida, 1972). Despite of their simplicity, these latter friction conditions are a good representation of the mechanical fault processes sustaining the evolution of a spontaneous rupture (Bizzarri & Cocco, 2003).

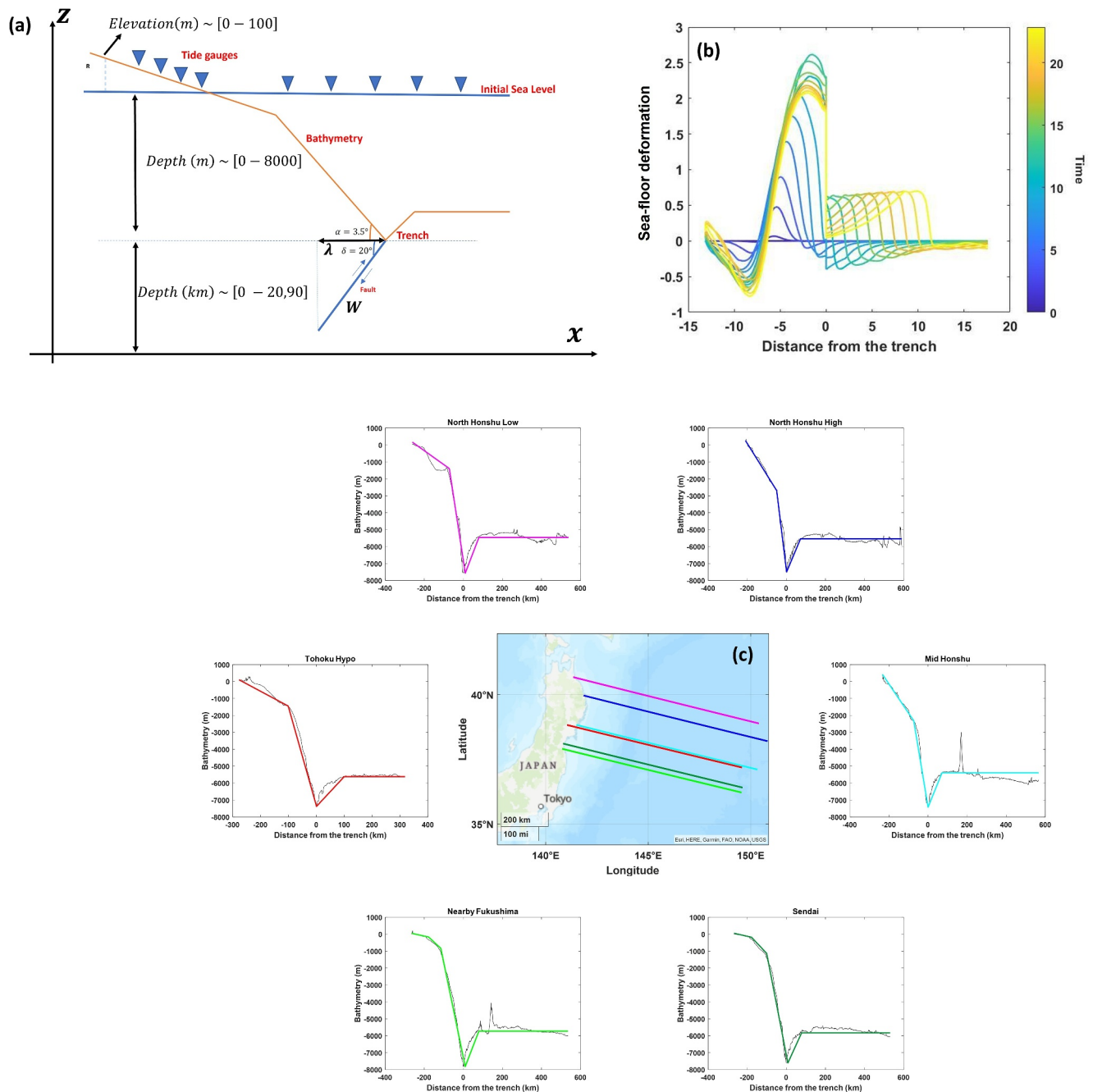


Figure 2. Schematic description of the simulation setup. (a) Sketch of the geometrical setup. The angle between the bathymetry (orange line) and the horizontal dashed line is exaggerated for sake of clarity with the ranges of the fault depth, bathymetry and elevation indicated beside the z -axis (note that the maximum fault depth ranges from 20 to 90 km depending on the source). The blue triangles represent the gauges where the wave amplitude is computed both inland and offshore. W and λ represent the width on the fault and the horizontal extent of the surface deformation respectively. (b) Time dependent vertical topo-bathymetric deformation as a function of the distance from the trench. The time increases from blue to yellow curves with a final static deformation featuring a lower maximum with respect to the transient deformation occurring earlier in the source history. All the variables are plotted as dimensionless normalized parameters. (c) Different modeled bathymetries. The modeled bathymetries are extracted from the 1D profiles in the map. Within the insets the bathymetry variation for each profile is plotted as a black line while the simplified geometry used in the simulations is plotted with the same color of corresponding profile in the map.

Elastodynamic equations with a sliding interface are numerically solved through a 2D Spectral Element Method (SEM, Komatitsch & Vilotte, 1998) where quadrangular elements are discretized using 9×9 Gauss-Lobatto-Legendre nodes, ensuring at least five points for the minimum propagating wavelength and at least four points to model the fault cohesive zone. This will ensure that the shrinking of the cohesive zone is physically well-

modeled as shown in Scala et al. (2017). The free surface is naturally modeled in SEM while the other boundaries mimic an infinite half-space through the implementation of Perfectly Matching Layers (PMLs, Festa & Vilotte, 2005).

A Newmark second order forward time scheme is implemented with an average Courant number of about 0.04. Such a small value allows to model the shallowest part of the domain honoring the shape of the domain between the fault and the free surface, and ensuring the stability also in the stretched elements within wedge-shaped intersection of the fault with the free surface.

The fault is modeled as a planar interface embedded in a homogeneous medium and forming a dip angle $\delta = 20^\circ$ with the horizontal direction similarly to what proposed by Scala et al. (2019). The free surface, in turn, is inclined of an angle $\alpha = 3.5^\circ$ with respect to the horizontal direction, this value being an average of the bathymetry slopes for the different profiles in the vicinity of the trench. Since we aim to model a simplified Tohoku-like environment in terms of fault geometry and topo-bathymetric distributions (see Section 3.2 for more details), the dip angle represents an average value between the almost horizontal trench and the steeper slope of the deep crust-mantle interface as shown in other works (Kozdon & Dunham, 2013; Murphy et al., 2018) implementing 1D extrapolations of Slab 2.0 modeling (Hayes et al., 2018).

The remote stress field is oriented to mimic the combination of a vertical lithostatic and a horizontal tectonic loading. Their components are compatible with a reverse frictional sliding mechanism as expected for interface subduction events. On the fault interface the initial normal traction $T_0^n(x, t)$ linearly increases to mimic the increase of lithostatic loading and the commonly observed elevated pore pressure on the inter-plate thrust (Huang et al., 2012; Murphy et al., 2016, 2018; Wendt et al., 2009). The static and the dynamic friction coefficients f_s and f_d are imposed to be equal to 0.25 and 0.05 respectively. The use of small values of friction limits the seismic wave-induced normal traction perturbation eventually preventing the opening at the free surface, as shown in Scala et al. (2019). The strength parameter $s = (f_s T_0^n - T_0^t) / (T_0^t - f_d T_0^n)$ is set to two on the entire interface to avoid the acceleration of rupture toward supershear regimes (Burridge, 1973), since it was never observed during the largest reverse subduction tsunamigenic earthquakes. To maintain the parameter s constant, the initial shear stress T_0^t increases with depth, following the linear increase of T_0^n with depth, similarly to what was shown in Scala et al. (2019). A cohesion c is imposed with a value of about 10% of the maximum stress. This cohesion decreases to zero in the close vicinity of the fault-free surface intersection to mimic a further increase of pore pressure (Murphy et al., 2018) and also avoiding inconsistency with the zero-traction condition.

To trigger the spontaneous crack, we defined an asperity featuring an initial shear stress larger than the shear strength and having a size L_c large enough to allow the rupture to move away from the nucleation zone (Uenishi & Rice, 2003). The nucleation asperity is placed at an intermediate depth with respect to the whole domain. Previous numerical experiments have shown that this is the preferential nucleation depth to generate events rupturing the whole domain and hence to describe the behavior of a megathrust earthquake (Murphy et al., 2018).

2.2. Tsunami Modeling

We used a multilayer shallow-water non-hydrostatic model. The multilayer approach was introduced by Audusse et al. (2011) and Fernández-Nieto et al. (2014) to capture vertical effects in shallow flows. The equations are depth-averaged at every layer, leading to a layer-wise constant approximation. Such a technique was already efficiently applied to landslide-generated tsunamis (Macías et al., 2021a) and for dry granular flows (Escalante, Fernández-Nieto, Garres-Díaz, & Mangeney, 2023). Concerning dispersion, following the pioneering work of Casulli (1999), non-hydrostatic effects are incorporated into the shallow water framework by splitting the total pressure into hydrostatic and non-hydrostatic components, providing a given profile for the non-hydrostatic component and the vertical velocity, together with the incompressibility condition. This approach has been recently further developed improving the dispersive layer-averaged approximations (Fernández-Nieto et al., 2018; Escalante, Fernández-Nieto, Garres-Díaz, Morales de Luna, & Penel, 2023), and efficiently GPU-implemented using finite volume and finite difference schemes (Escalante et al., 2018). In order to increase the accuracy of the model, we consider the nonlinear non-hydrostatic system introduced in Fernández-Nieto et al. (2018). The system is obtained after discretizing the fluid into several layers and a depth-

averaged approximation of the Euler equations. As the number of layers is increased, the system can adequately describe the vertical structure of the flow. Formally speaking, the solution of the multilayer system converges to the weak solutions of the inviscid incompressible Euler equations (Fernández-Nieto et al., 2014). Moreover in Fernández-Nieto et al. (2018) the dispersive properties of a linearization of the system are verified. This latter linear study shows that the linear dispersive relation of the system converges uniformly to the one given by the Stokes linear theory when the number of layers tends to infinity. The nonlinear multilayer system is written as:

$$\begin{aligned} \partial_t h + \partial_x(h\bar{u}) &= 0, \\ \partial_t(h_\alpha u_\alpha) + \partial_x(h_\alpha u_\alpha^2) + gh_\alpha \partial_x \eta + u_{\alpha+1/2} \Gamma_{\alpha+1/2} - u_{\alpha-1/2} \Gamma_{\alpha-1/2} \\ &= -\frac{1}{2} h_\alpha \partial_x (p_{\alpha+1/2} + p_{\alpha-1/2}) + (p_{\alpha+1/2} - p_{\alpha-1/2}) \partial_x z_\alpha + K_{\alpha-1/2} - K_{\alpha+1/2} - m_\alpha^u, \\ \partial_x(h_\alpha w_\alpha) + \partial_x(h_\alpha w_\alpha u_\alpha) + w_{\alpha+1/2} \Gamma_{\alpha+1/2} - w_{\alpha-1/2} \Gamma_{\alpha-1/2} &= -h_\alpha (p_{\alpha+1/2} - p_{\alpha-1/2}) - m_\alpha^w. \end{aligned} \quad (3)$$

In system Equation 3, $h(x,t)$ represents the total water height at each point $x \in \Omega \subset \mathbb{R}$, and time $t \geq 0$, where Ω is the considered (horizontal) domain. The water height is decomposed along the vertical axis into a prescribed number of layers $L \geq 1$ (Figure 1). For any layer α , its thickness will be assumed to be $h_\alpha = l_\alpha h$, for some values $l_\alpha \in (0,1)$ such that $\sum_{\alpha=1}^L l_\alpha = 1$. Usually, $l_\alpha = 1/L$ is selected. The upper and lower interfaces of the layer α are represented by $z_{\alpha+1/2}$ and $z_{\alpha-1/2}$, respectively, that is, $z_{\alpha+1/2} = z_b + \sum_{\beta=1}^\alpha l_\beta h$. The uppermost interface corresponds to the sea surface, denoted by $\eta(x,t) = h(x,t) + z_b(x,t)$; the lowermost one corresponds to the seafloor basin represented by $z_b(x,t)$, which is supposed to be perturbed by the earthquake. Finally, $z_\alpha = \frac{1}{2}(z_{\alpha-1/2} + z_{\alpha+1/2})$ denotes the level of the middle point of the layer. The depth-averaged velocities in the horizontal and vertical directions are written as $u_\alpha(x,t)$, and $w_\alpha(x,t)$, respectively. Finally, $p_{\alpha+1/2}$ denotes the non-hydrostatic pressure at the interface $z_{\alpha+1/2}$, and is assumed to be 0 at the free surface. The mean of the depth-averaged horizontal velocities is indicated by $\bar{u} = \sum_{\alpha=1}^L l_\alpha u_\alpha$.

Moreover, for any field $f \in \{u, w\}$, we denote $f_{\alpha+1/2} = \frac{1}{2}(f_{\alpha+1} + f_\alpha)$. As usual $g = 9.81 \text{ m/s}^2$ is the gravity acceleration and $\Gamma_{\alpha+1/2}$ parametrizes the mass transfer across interfaces:

$$\Gamma_{\alpha+1/2} = \sum_{\beta=\alpha+1}^L \partial_x (h_\beta (u_\beta - \bar{u})), \quad (4)$$

where we assume no mass transfer through the seafloor or the free surface ($\Gamma_{1/2} = \Gamma_{L+1/2} = 0$). Each layer is supplemented with the following divergence-free constraint $\mathcal{I}_\alpha = 0$, $\alpha \in \{1, 2, \dots, L\}$,

where

$$\begin{aligned} \mathcal{I}_\alpha &= h\alpha \partial_x u_\alpha + 2\bar{w}_{\alpha+\frac{1}{2}} - 2w_\alpha, \\ \bar{w}_{\alpha+\frac{1}{2}} &= \partial_t z_b + u_\alpha \partial_x z_{\alpha+1/2} - \sum_{\beta=1}^\alpha \partial_x (h_\beta u_\beta), \end{aligned} \quad (5)$$

and the term $\partial_t z_b$ accounts for the movement of the bottom interface.

It is worth to highlight that the features of the model are improved by adding extra dissipation terms accounting for friction with the bottom (m_α^u), for viscous terms that model the shear stresses between the layers ($K_{\alpha\pm 1/2}$), and for the breaking of the waves near the coast (m_α^w). Here, we used the following dissipation models proposed by Macías et al. (2021a).

For the friction effects between the water and the seafloor, we used a standard Gauckler-Manning friction formula applied to the lowest layer

$$m_{\alpha}^u = \begin{cases} gLn^2|u_1| \frac{hu_1}{h^{4/3}}, & \alpha = 0 \\ 0, & \alpha \in \{2, \dots, L\} \end{cases} \quad (6)$$

We followed a simplified version of the model presented in Bonaventura et al. (2018) for the shear stress between the layers

$$K_{\alpha+1/2} = -\nu \frac{u_{\alpha+1} - u_{\alpha}}{(h_{\alpha+1} + h_{\alpha})/2} \quad (7)$$

where ν is a constant kinematic viscosity, and $K_{1/2} = K_{L+1/2} = 0$.

For the breaking dissipation model, we considered here an extension of the simple, efficient, and robust model considered in Escalante et al. (2019) for a two-layer model:

$$m_{\alpha}^w = C w_{\alpha} |\partial_x(hu_{\alpha})|, \quad \alpha \in \{1, \dots, L\} \quad (8)$$

The coefficient $C(x,t)$ defines breaking criteria to switch on/off the dissipation of the energy due to the presence of a breaking wave (e.g., Roeber et al., 2010). Here, we used

$$C = \begin{cases} 35 \left(\frac{|\bar{u}|}{0.4\sqrt{gh}} - 1 \right) & \text{if } |\bar{u}| > 0.4\sqrt{gh}, \\ 0 & \text{if } |\bar{u}| \leq 0.4\sqrt{gh}. \end{cases} \quad (9)$$

The system in Equations 3–5 satisfies an energy balance equation (Fernández-Nieto et al., 2018). The used modeling includes the non-hydrostatic ocean response and accurately captures dispersion and related effects during tsunami propagation and generation (Ma et al., 2012; Macías et al., 2021a, 2021b). Using a standard, Stokes-type, Fourier analysis for the linearized version of Equations 3–5 around the water at rest (steady-state), the phase, group velocities, and linear shoaling gradient are determined and compared with the Airy or Stokes linear theory for different numbers of layers (see Figure S1 in Supporting Information S1, where relative errors are shown for the phase and group velocities, as well as for the shoaling gradient). One can prove uniform convergence for the analytical values when the number of layers increases (Fernández-Nieto et al., 2018).

A detailed description of the numerical discretization and implementation of this model, along with the comparison of results with standard benchmark problems and laboratory experiments, are presented in Text S1 and Text S2 of Supporting Information S1.

3. Numerical Setup and the Simulated Data Set

3.1. Earthquake Rupture Modeling

The earthquake-tsunami coupled simulations are here performed using the time-dependent vertical displacement on the free surface, generated by a dynamic rupture, as a generation mechanism for a tsunami simulation (Figure 2a).

Given the simplicity of the geometrical model, by running a single rupture dynamic simulation and properly normalizing the input/output physical quantities, it is possible to define a set of different earthquake scenarios featuring realistic source parametrization. In particular, the slip on the fault δu and the ensuing displacement on the surface d (both vertical and horizontal components) are normalized by means of the critical slip weakening distance leading to the dimensionless quantities $\tilde{\delta u} = \delta u/D_c$ and $\tilde{d} = d/D_c$. All the tractions T are normalized through the maximum stress drop on the fault $\Delta\sigma_0$ as $\tilde{T} = T/\Delta\sigma_0$. All the distances z and x modeled in the simulation domains, in particular the fault extent W and the ensuing tsunami source size λ (See Figure 2a), and the time t are normalized as $\tilde{z} = \frac{\Delta\sigma_0}{\mu D_c} z$ and $\tilde{t} = \frac{V_s \Delta\sigma_0}{\mu D_c} t = \frac{\Delta\sigma_0}{V_s \rho D_c} t$, respectively. In these two latter normalization factors, μ and ρ are the medium rigidity and density, respectively, with $V_s = \sqrt{\mu/\rho}$ the S-wave propagation velocity. The

Table 1
Input Parameters for the Performed Earthquake Rupture Simulation

V_s (km/s)	ρ (g/cm ³)	D_c (m)	$\Delta\sigma_0$ (MPa)
1.0	1.0	3.0	0.86

normalized quantities are the solutions of the dimensionless formulation of Equations 1 and 2 and this setup allows us to define an ensemble of different earthquake and tsunami sources featuring a broad range of source extents and durations through the selection of the parameters D_c , $\Delta\sigma_0$, V_s and ρ in realistic ranges constrained, as explained in what follows, by seismological observations and elastic properties of media. The equivalence between dimensional

and dimensionless equations and between full simulations and re-scaled solutions is shown in Text S3 and Figure S8 in Supporting Information S1.

The parameters used in the performed simulation are listed in Table 1, and results are shown in Figure 2b, in terms of dimensionless sea floor deformation at various dimensionless time steps. In the simulation, we considered a Poisson's coefficient $\nu = 0.25$, hence the P-wave velocity $V_p = \sqrt{3}V_s$. The distance from the trench is along the horizontal direction. It is worth noticing that the final static deformation (yellow curve in Figure 2b) might feature a lower maximum amplitude with respect to the transient deformation occurring earlier during the source time evolution (green curves in Figure 2b). This effect is due to the surface deformation induced by the surface reflected waves interacting with the fault, while the seismic rupture is approaching the surface itself, as already shown by Oglesby et al. (2000) and Scala et al. (2019). The singularity, in seafloor displacement (see Figure 2b) around the trench is due to the fact that the modeled rupture reaches the surface and this generates a scarp at the interface. Beyond the scarp, a secondary vanishing deformation with a maximum amplitude of about 25% of the final static displacement, due to the rightward propagating seismic waves, triggers a tsunami wave propagating rightward from the trench ahead of the main wave.

Starting from the normalized outputs of the seismic rupture simulation, a broad range of different earthquake sources can be modeled. To this aim: (a) we select different values for the shear wave velocity V_s and the density ρ of the medium and for the stress drop $\Delta\sigma$, within ranges compatible with seismological observations; (b) we re-scale the dimensionless outputs, obtaining the source characteristic duration, hereinafter τ , the maximum amplitude d , and the along-dip extent W , for each selection of V_s , ρ and $\Delta\sigma_0$ (See Table S2 in Supporting Information S1). (c) Finally, as detailed later in Section 3.2, from each modeled rupture the tsunami source time evolution and the characteristic wavelength are estimated.

We select shear wave velocity (V_s) and density (ρ) values to cover a broad range of elastic properties which typically characterize the slabs at the characteristic seismogenic depths. V_s ranges between 350 and 4,700 m/s while ρ ranges between 1,850 and 3,400 kg/m³ with the rigidity being $\mu = V_s^2 \cdot \rho$. These values are sampled integrating values from reports released by Earthquake Research Promotion of Japanese Government (Earthquake Research Committee, 2017 with densities extrapolated through Ludwig et al., 1970) and from several tomographic models for the Japanese slab (e.g., Miyake et al., 2008; Takahashi et al., 2004; Yamada & Iwata, 2005). The 23 sampled shear wave velocity, density and rigidity values and the corresponding subduction layers, are reported in Table S1 of Supporting Information S1.

The stress drop values are sampled in a range between 0.2 and 30 MPa according to general observations about crustal, downdip interplate and tsunami earthquakes (Abercrombie et al., 2017; Bilek et al., 2016; Folesky et al., 2021; Kanamori & Brodsky, 2004; Venkataraman & Kanamori, 2004). Within this range, we select 15 values equally spaced on a logarithmic scale.

A single characteristic slip weakening distance is selected ($D_c = 2$ m) leading to a maximum slip $\delta u \sim 15$ m for the re-scaled rupture dynamic simulation. This value is consistent with the one extrapolated for a $M_w = 9.0$ event according to the scaling law proposed by Skarlatoudis et al. (2016).

By combining all the sampled parameters, up to 345 different earthquake source models might be created. However, most of them lead to either unrealistic or out of range of interest seismic source size. The smallest rigidity values cannot be associated indeed with large stress drops and vice versa, to avoid modeling too small and too large earthquakes, respectively. Imposing a range of fault widths compatible with the expected value ($\pm 1\sigma$) of the scaling relations proposed by Strasser et al. (2010) for a magnitude interval $8.0 \leq M_w \leq 9.0$, we select 81 out of the 345 combinations of parameters (See Table S2 and Figure S9a in Supporting Information S1). In particular, we highlight that the smallest value of rigidity (see line one in Table S1 in Supporting Information S1) is never used for the tsunami modeling.

Each parameter combination leads to a characteristic source duration $\tau = \tau' \mu D_c / (\Delta \sigma V_r)$ and to an along-dip source size $W = W' \mu D_c / \Delta \sigma$, with $\tau' = 17.1$ and $W' = 8.3$ representing the dimensionless duration and width derived from the dynamic rupture simulation. By dividing W by τ an average rupture velocity V_r can be estimated (Figure S9b in Supporting Information S1). The rupture duration ranges between 25 and 570 s, while $0.2 \text{ km/s} \leq V_r \leq 2.3 \text{ km/s}$, these values are consistent with the common observations for recent tsunamigenic earthquakes (Ye et al., 2016; Yoshimoto & Yamanaka, 2014). In the next sections, all the results will be presented as a function of τ , W and the ratio τ/W that is the rupture duration normalized by the size representing a measure of how slow the rupture evolution with time is. Some of the results will be also presented as a function of $\lambda = W \cdot \cos(\text{dip}) = W \cdot \cos(20^\circ)$ (refer to the sketch in Figure 2a). This latter quantity is the horizontal maximum extent of the seismic source and, within this simple geometrical model, it scales with the characteristic wavelength of the tsunami source. The longest durations owe to small values of rigidity and stress drops, in turn deriving from shallow-depths rheological conditions, while the fastest sources are associated with large values of rigidity and stress drop, a more realistic condition for deeper events (Bilek & Lay, 1999; Ebeling & Okal, 2012; Geist & Bilek, 2001; Okal et al., 2016). Within this framework, the choice of a logarithmic scale for the stress drop along with the large number of models featuring small rigidity values (Table S2 in Supporting Information S1) allows us to more finely sample sources characterized by longer duration. Such slow sources are expected to be poorly modeled using an instantaneous source approach. As a further test, we compute the moment magnitude $M_w = \frac{2}{3}(\log_{10} M_0 - 9.1)$ for each of the 81 modeled sources, with $M_0 = \mu \langle \delta u \rangle LW$ being the seismic moment. The rigidity μ and the width W are the values listed in Table S2 in Supporting Information S1, the average slip $\langle \delta u \rangle$ is estimated from the re-scaled rupture simulation and the length L is estimated to be consistent with W according to Strasser et al. (2010) scaling law. The estimated M_w values are in the range [7.2, 9.3], which is consistent with the a priori constraints.

3.2. Tsunami Simulations

The time-dependent vertical seafloor deformations for each of the re-scaled rupture models are used as generation mechanism for the tsunami simulations. In particular the above mentioned quantities λ and τ are used to represent the size and the duration of the tsunami source respectively. The maximum amplitudes d only depends on D_c , whose value is the same for all the earthquake models. Hence the maximum amplitudes are $d_{max} = 5.2 \text{ m}$ and $d_{max} = 4.5 \text{ m}$ for all the time-dependent and instantaneous simulations respectively, with the time-dependent models featuring the transient maximum described in Section 3.1. The intersection between the fault and the seafloor coincides with the deepest point of the bathymetry at the trench (see the sketch in Figure 2a). The zero height of the bathymetry represents the initial sea level while the positive values represent the topographic elevation of the coast. The sea surface elevation for all the grid points, both offshore and inland, is recorded each 30 s. For all simulations, 2 hr of tsunami time evolution are modeled.

We consider the time-dependent 3-layer non-hydrostatic model (hereinafter TD-NH) as the reference and we compare against it the simplified models (instantaneous source and shallow water, hereinafter IS and SW respectively). For the aim, we simulate each initial condition 4 times (TD-NH, IS-NH, TD-SW and IS-SW). The IS are simulated imposing an instantaneous seafloor deformation equals to the final static displacement (as the yellow curve in Figure 2b). SW is simulated through a single layer hydrostatic approximation, and we use a Manning friction coefficient equal to 0.025 for all the simulations. A constant Courant number equal to 0.9 is imposed. All these choices are justified by the performed tests, described in sections Text S1 and Text S2 in Supporting Information S1.

The comparison is performed through three metrics: the wave amplitude η (sea surface elevation with respect to the still water level) and its maximum η_{max} at offshore gauges, the flow-depth D and its maximum D_{max} at onshore gauges (the water amplitude onto the topographic elevation) and the maximum runup R_{max} that is the maximum topographic elevation reached by the tsunami during the inundation. For any metrics K , we define the discrepancy ΔK as the relative error due to the use of a simplified model:

$$\Delta K = \frac{K_{ref} - K_{simpl}}{K_{simpl}} \quad (10)$$

ΔK might assume negative values indicating that a simplified model produces an overestimation with respect to the reference one.

To investigate how much the results depend on the coupling between the tsunami and the oceanic and coastal morphology, the initial deformations are projected onto 6 different 1D topo-bathymetric profiles (colored lines on the map of Figure 2c). Each profile (blue lines in the insets around the map in Figure 2c) is extracted from the 30 arc-sec model SRTM30+ (https://topex.ucsd.edu/www_html/srtm30_plus.html) and then simplified to obtain piece-wise linear depth variations (colored profiles in the insets of Figure 2c) characterized by a planar scarp combined with either a planar or a segmented shelf toward and beyond the coast. This simplification allows to limit the effect of short size discontinuities and to provide general considerations about the effect of steep, flat and intermediate bathymetric profiles in the vicinity of the coast. The scarp slopes are quite similar to each other and are characterized by an average angle of 3.5° among the 6 profiles. Conversely, in the vicinity of the coast, the slopes are gentler in the southern part of the Tohoku region (Sendai and Fukushima areas), and steeper in the northern part (Iwate prefecture) with an intermediate behavior along the profile containing the nucleation area of the Tohoku earthquake. The mainland is modeled as a single slope. Most of the results presented in the next section will be obtained for the Tohoku nucleation area (red profile and bathymetry in Figure 2c) while a comparison between the different bathymetries is shown in Section 4.3.

To ensure enough spatial resolution we performed a preliminary convergence test, running equivalent simulations on 6 grids characterized by different space sampling $\Delta x = [500 \text{ m}; 250 \text{ m}; 125 \text{ m}; 62.5 \text{ m}; 31.25 \text{ m}; 15,625 \text{ m}]$. We tested the discrepancy of each grid with respect to the finer one (assumed as a reference) computing the $\Delta\eta_{max}$ offshore and the ΔD_{max} on the coast similarly to Equation 10 but considering the module of the difference as numerator and the value on the finest grid as denominator. With this definition the Δ values represent the relative errors due to the use of a rougher grid. This analysis has been carried out extracting η_{max} and D_{max} at fixed gauge positions (regardless of the time at which these maxima are recorded) for two end-member initial conditions that is the largest size event (ID 1 in Table S2 in Supporting Information S1, $W = 275.3 \text{ km}$) and the smallest size one (ID 81 in Table S2 in Supporting Information S1 $W = 57.06 \text{ km}$) respectively. We retrieved $\Delta\eta_{max} < 5\%$ everywhere and for both tests, already with rather rough grids (up to $\Delta x = 125 \text{ m}$ offshore and $\Delta x = 62.5 \text{ m}$ in the vicinity of the coast, Figures S10c and S10d in Supporting Information S1). However, ΔD_{max} is below the threshold only for $\Delta x = 31, 25 \text{ m}$ in the vicinity of the maximum runup position at least for the smallest size simulations (see Figure S10a in Supporting Information S1). Since one of our aims is to model with enough accuracy the inundation and the maximum runup, we finally used $\Delta x = 31, 25 \text{ m}$ for the whole simulation data set.

4. Results

4.1. Off-Shore and Coastal Wave Amplitude

4.1.1. Time-Dependent Versus Instantaneous Source

First, we show a qualitative comparison between the water waves generated by the non-hydrostatic time-dependent (TD-NH) and instantaneous sources (IS-NH).

Figure 3 shows the wave amplitude as a function of the distance from the trench for two different initial conditions (simulations ID 31 and 11 are plotted on the left and right columns, respectively, see Table S2 in Supporting Information S1) at different time steps and for both TD-NH and IS-NH. While the two simulations are characterized by the same τ/W value and hence by an equivalent evolution over time, the simulations on the right panels (Figures 3b, 3d and 3f) feature a large enough W (and τ) to generate coastal subsidence. For both simulations (small and large W), the TD sources feature a larger maximum wave amplitude than the corresponding IS, and the maxima occurs at various times, as an effect of the different duration of the transient. However, this transient is rapidly attenuated during the landward propagation outside of the source region, and, starting from a certain time, the IS systematically features larger η_{max} with respect to the TD simulation (Figures 3e and 3f). Conversely, toward the open sea, rightward from the trench, we retrieve the opposite behavior with the TD source leading to larger yet delayed maximum η as an effect of the directivity (the seaward motion of the upper plate).

Regardless of the source temporal features (TD vs. IS), the main difference between simulations with small and large W emerges while the waves are approaching the coast. For small W , such that λ is smaller than half distance between trench and the coast (Figures 3a, 3c and 3e), the wave shoals. For larger ruptures (Figures 3b, 3d and 3f), the instantaneous sea drawback limits the shoaling and thus the amplification of the wave close to the coast as can be spotted by comparing Figures 3e and 3f.

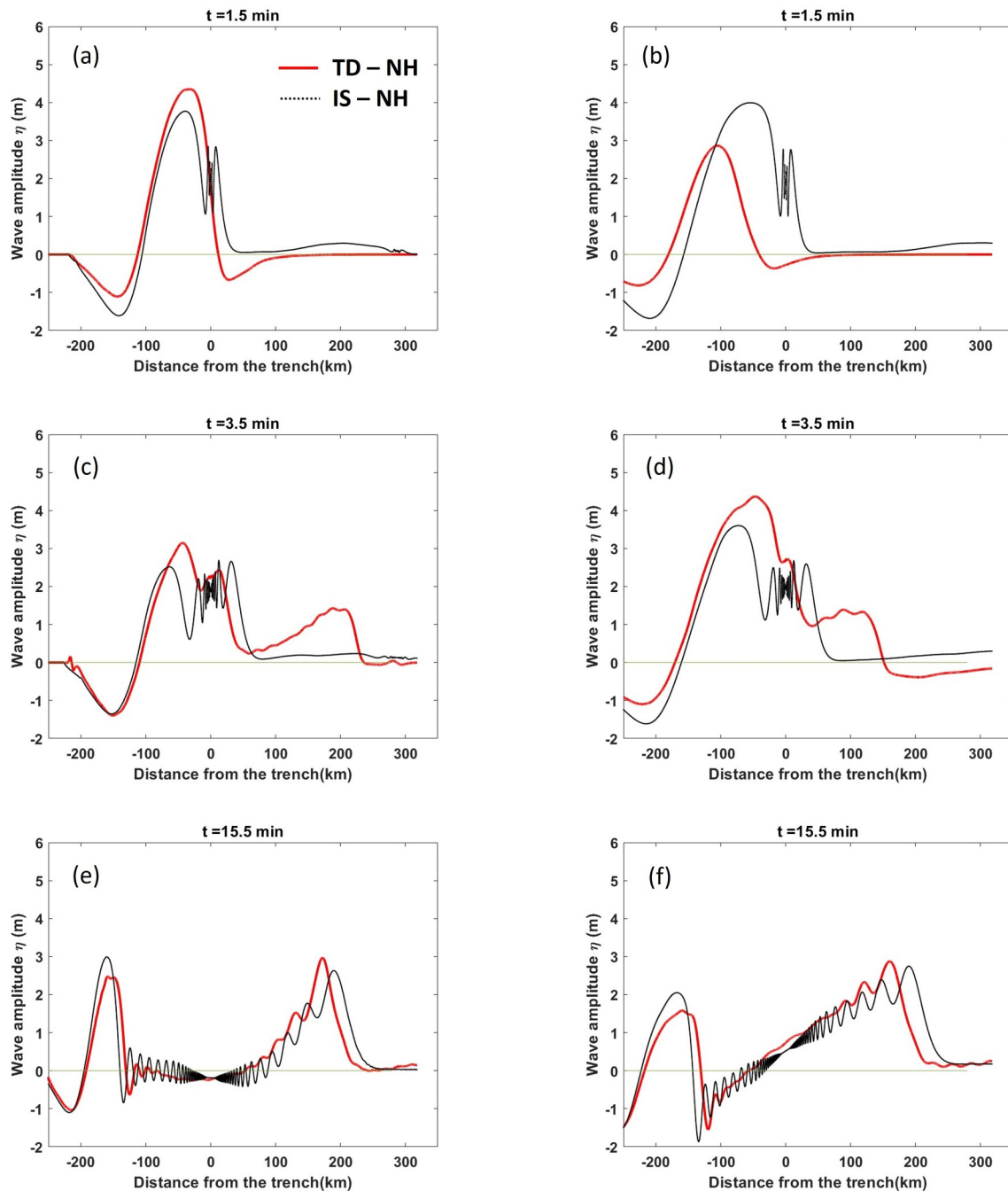


Figure 3. Wave amplitude as a function of the distance from the trench for TD—NH (red curves) and IS—NH (black dotted lines) at three different time steps and for two simulations: the ID 31 (left panels) and the ID 11 (right panels) in Table S2 in Supporting Information S1. These simulations represent examples of small and large-size sources, respectively. The whole evolution can be found in the Supporting Information (Movies S1 and S2).

This difference is evident also by focusing on wave evolution around and on the coastline (Figure 4) at a later stage ($t > 40$ min). From this close-by view, it can also be seen that the inundation begins earlier for rupture with large W (Figure 4b), when for the small W simulation, the tsunami is still in the shoaling phase (Figure 4a). When the large source simulation has almost reached its maximum (Figure 4d), the inundation for the smaller source starts (Figure 4c), reaching in the end a maximum runup that is about 1.5 times the one for the large W , for both IS and TD sources. This is a direct consequence of the potential energy accumulation during the shoaling process (Figures 4e and 4f). However, independently of the size and duration of the TD source, approximating it with an

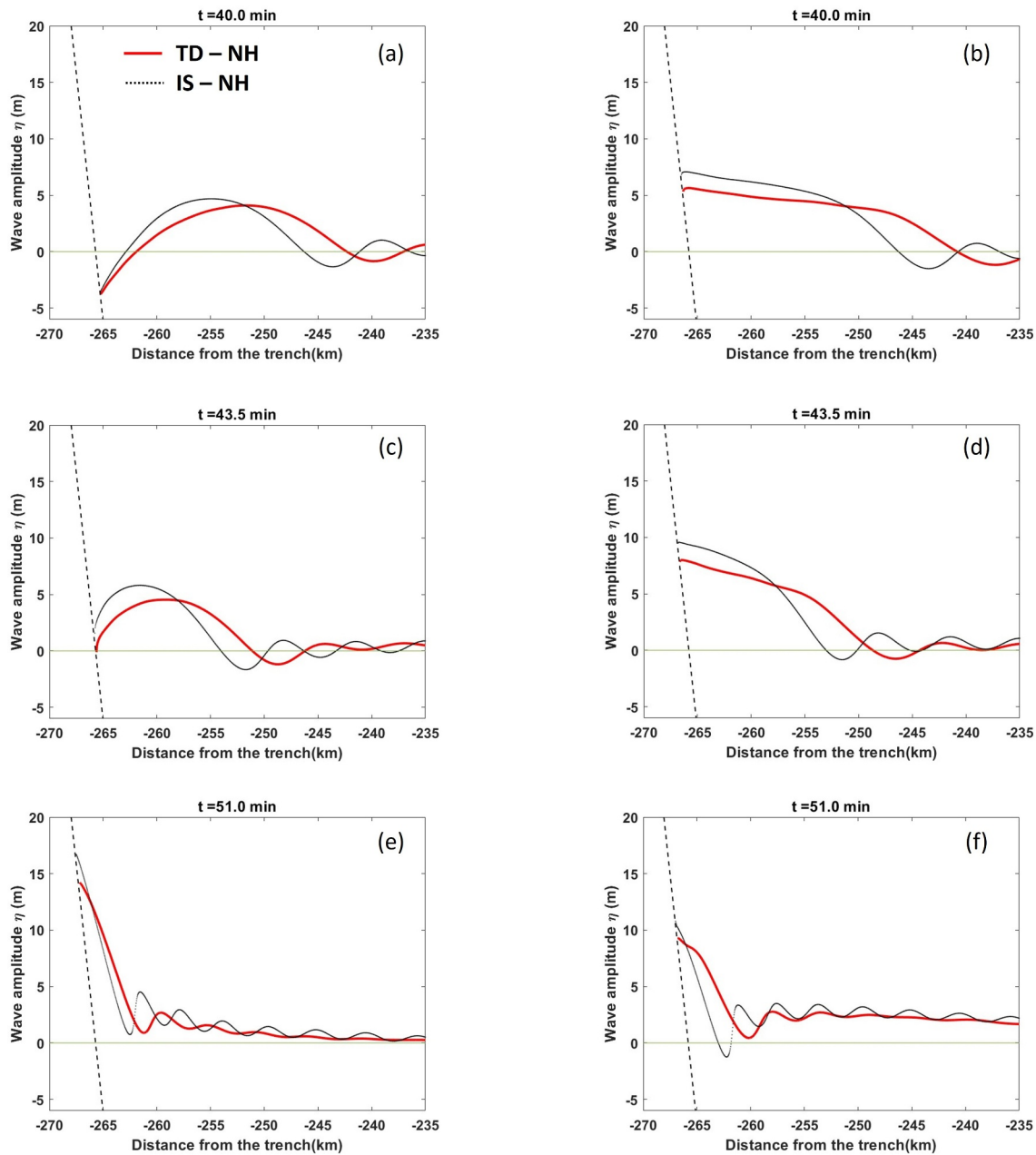


Figure 4. Wave amplitudes, at the coast, as a function of the distance from the trench for TD—NH (red curves) and IS—NH (black dotted lines) at three different time steps and for two simulations: the ID 31 (left panels) and the ID 11 (right panels) in Table S2 of Supporting Information S1. These simulations represent examples of small and large size sources respectively. The short-dashed line on the left represents the coastline within each panel. The whole evolution can be found in the Supporting Information (Movies S3 and S4).

instantaneous source always results in larger flow-depth D , at all the inundated points on the coast, and maximum runup R_{max} .

To systematically quantify the discrepancy between the IS and TD sources, we investigated the variability of ΔD_{max} at the points on the coast (Equation 10), as a function of τ/W (horizontal axis) and λ (different colors) for all the 81 simulations (see Section 3 and Table S2 in Supporting Information S1). In Figure 5 the results for the first point on the coast are summarized. We observe that the IS source systematically overestimates the flow-depth (ΔD_{max} values are always negative, Figure 5a). The slower the TD rupture, the larger the discrepancy with the corresponding IS simulation. A second trend depending on the source extension emerges, as for fixed τ/W , larger

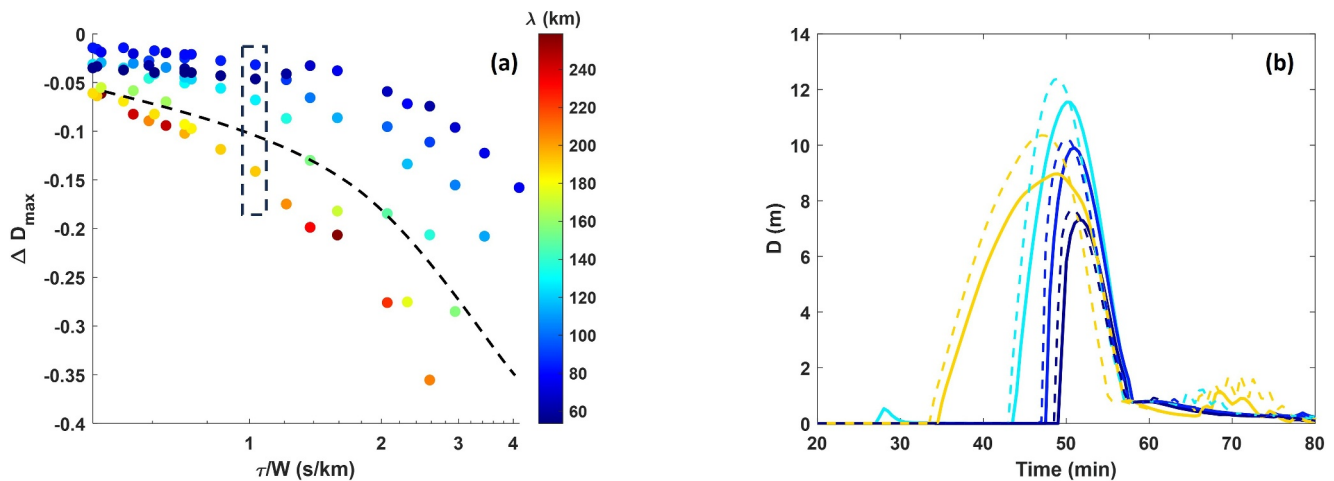


Figure 5. Relative discrepancy between time-dependent (TD-NH) and instantaneous source (IS-NH) results in terms of flow-depth at the first point on the coast (a) ΔD_{max} at the first point on the coast as a function of τ/W with color scale marking the source horizontal extension λ . The black dashed line separates the two highlighted trends for small and large ruptures. (b) Flow-depth as a function of time for the four simulations within the black-dashed rectangle in panel (a) plotted with the same colors. In panel (b) TD and IS sources are represented through solid and dashed lines respectively.

ruptures lead to larger discrepancies. A comparison between the time histories of the flow-depths at the first point on the coast is shown in Figure 5b, for the simulations inside the dashed rectangle in Figure 5a. The four simulations are characterized by the same source evolution with time that is τ/W , with the larger extension due to a larger stress drop $\Delta\sigma$. The flow-depth amplitude D_{max} increases with λ until a maximum value (cyan curves in Figure 5b) with an overestimation between 3% and 7% due to the instantaneous modeling. For larger λ , D_{max} decreases featuring larger overestimations up to about 14%. This overestimation is particularly significant for the largest λ values, because the inundation directly relates with source time history which becomes dominant given the virtual absence of landward propagation and shoaling. We verified that comparable results hold when a SW propagation modeling is used, which is important because the most commonly adopted approximation is the SW-IS approach (Figure S11 of Supporting Information S1).

4.1.2. Non-Hydrostatic Versus Shallow Water Propagation

To perform a systematic comparison between the accuracies of NH and SW propagation schemes in modeling a tsunami generated by a TD seismic source, we run a set of SW propagation simulations of tsunamis triggered by the same seismic TD source as used in the NH simulations described in the previous section.

Figures 6a and 6b show the $\Delta\eta_{max}$ for two gauges located between the source and the coast and beyond the trench respectively, while in Figure 6c the ΔD_{max} is shown for the first point on the coast. Even though for the smallest modeled source, λ is more than 7 times larger than the maximum sea-floor depth, and hence the SW limit is quite far to be violated (Abrahams et al., 2023), significant $\Delta\eta_{max}$ with negative values down to -30% occurs, indicating that SW systematically overestimates the NH wave amplitude during the coastward propagation (Figure 6a). For the slowest and smallest ruptures, the $|\Delta\eta_{max}|$ is enhanced as an effect of short wavelength oscillations affecting both the primary and the secondary waves. Such oscillations are due to coupling of the dynamic evolution of the source with the instantaneous dissipative shock introduced by the SW propagation (see wave evolution in left panels of Figure S12 in Supporting Information S1).

For smaller ruptures, a similar SW overestimation emerges also in the open ocean propagation beyond the trench, while a systematic underestimation emerges at intermediate and large source sizes λ as shown in Figure 6b.

However, such differences affect to a lesser extent the flow-depth maximum amplitude on the coastal points with only few very slow simulations featuring a $|\Delta D_{max}|$ slightly larger than 0.1, as evidenced in Figure 6c for the slowest ruptures.

Modeling NH and SW regimes with IS instead significantly reduces $|\Delta\eta_{max}|$ offshore (Figures S13a and S13b in Supporting Information S1) and $|\Delta D_{max}|$ on the coast (Figure S13c in Supporting Information S1) for small source

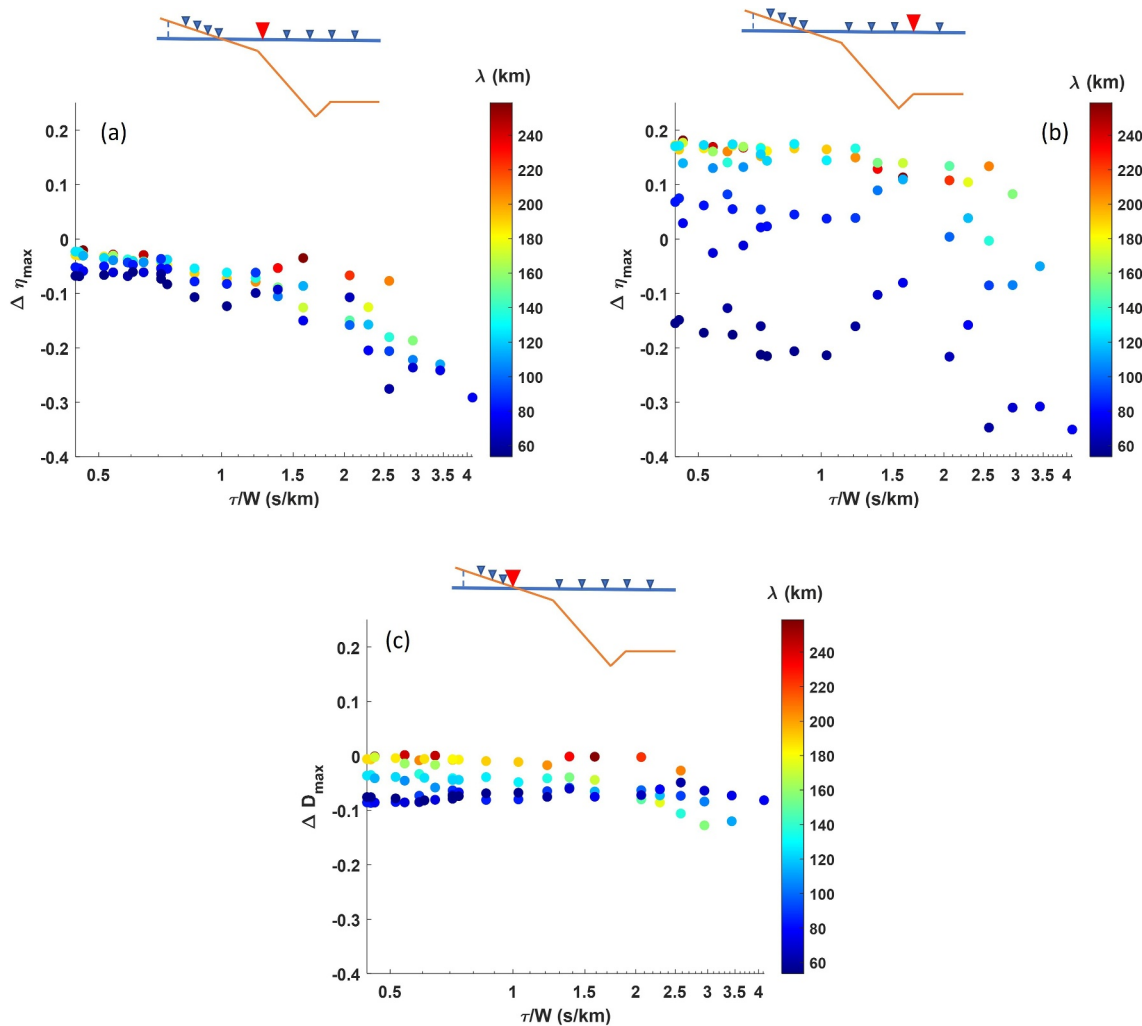


Figure 6. Relative discrepancy between Non-Hydrostatic (NH) and Shallow Water (SW) results when TD sources are used for both propagation regime. (a) $\Delta \eta_{max}$ at a gauge placed along the coastward propagation as a function of τ/W with color scale marking the source horizontal extension λ . (b) $\Delta \eta_{max}$ at a gauge placed rightward beyond the trench as a function of τ/W with color scale marking the source horizontal extension λ . (c) ΔD_{max} at the first point on coast as a function of τ/W with color scale marking the source horizontal extension λ . For sake of comparison the figures are plotted with the same scale. A sketch of the position of points where the Δ are computed is plotted within each panel.

size λ , while the SW underestimation for intermediate and large λ values, beyond the trench, is characterized by similar $\Delta \eta_{max}$. Despite in this condition the maximum amplitude metrics being overall convergent, an interesting feature emerges following the waveform evolution with time for the secondary waves. Indeed, when an instantaneous source is modeled, the NH propagation generates high-frequency oscillations behind the primary wave possibly hampering the correct modeling of secondary waves eventually generated by the dispersive propagation regime (Figure S14 in Supporting Information S1). In other words, in the case of instantaneous ruptures with strong gradients, a singularity is generated on seafloor. The propagation of this singularity generates a train of secondary waves that overlap the dispersive waves. Such effect has been confirmed by laboratory experiment and convergence tests, performed with a refined grid and modeling 5 and 7 non-hydrostatic layers.

4.2. Maximum Runup

To address how the modeling approximations affect the tsunami evolution on the coast, we used the maximum runup R_{max} and ΔR_{max} as metrics. We performed similar comparisons as for the amplitude, first between the TD-NH and IS-NH, and then between TD-SW and TD-NH. We show the results also for IS-SW.

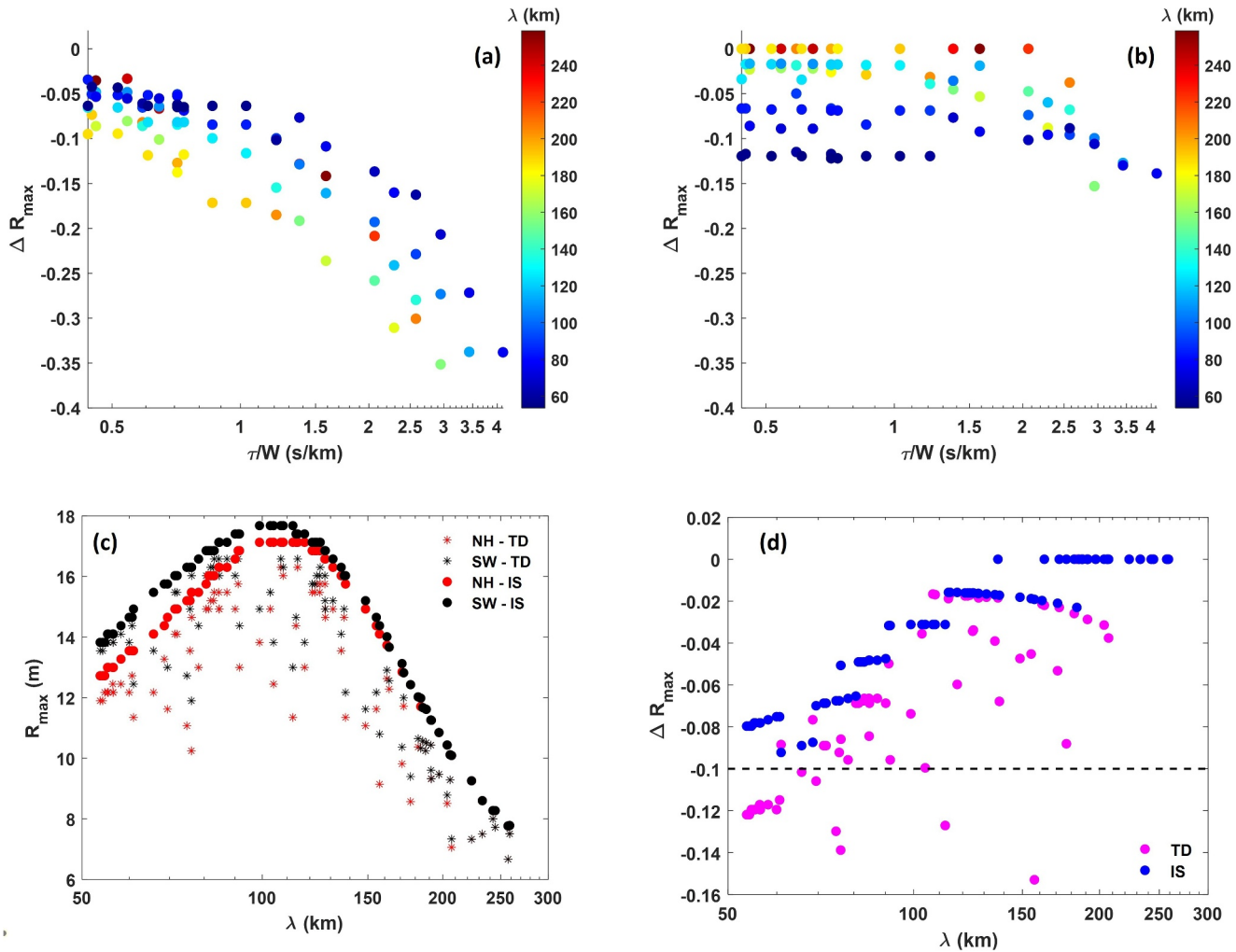


Figure 7. Maximum runup R_{max} comparison between the four different models (TD-NH, IS-NH, TD-SW, IS-SW). (a) ΔR_{max} between TD-NH and IS-NH as a function of τ/W with color scale marking the source horizontal extension λ . (b) ΔR_{max} between TD-NH and TD-SW as a function of τ/W with color scale marking the source horizontal extension λ . For sake of comparison, the Figures in panels (a) and (b) are plotted with the same scale. (c) R_{max} on the coast as a function of λ for the four different models (d) ΔR_{max} as a function of λ with blue and magenta dots referring to IS-NH versus IS-SW and TD-NH versus TD-SW comparison, respectively. The dashed line indicates that only for TD sources some simulations feature $|\Delta R_{max}| > 0.10$.

Figure 7a shows the ΔR_{max} for IS-NH taking TD-NH as a reference, as a function of τ/W and λ . A trend similar to the one shown in Figure 5a is observed, with an increasing discrepancy for slower and larger ruptures. However, the largest ruptures generate significantly smaller values of both R_{max} and ΔR_{max} as a consequence of the significant subsidence that completely prevents the shoaling limiting the runup. When the same comparison is performed between TD-NH and TD-SW, we retrieved smaller discrepancies with maximum values of ΔR_{max} around the 16% for the smallest modeled sources (Figure 7b). A negligible contribution to the discrepancy is associated to the parameter τ/W , which emerges only for very slow ruptures ($\tau/W > 3$ s/km equivalent to an average rupture velocity $V_r \sim 330$ m/s).

The absolute R_{max} behavior for all the 81 simulations and for the 4 models is summarized in Figure 7c evidencing a resonant character as a function of λ . The resonance is clearly visible for IS cases, with an optimal amplification for a narrow λ range, around 100–120 km. For TD sources, both for SW and NH, R_{max} is also influenced by the source duration leading to a scattered R_{max} pattern against λ still following the resonant trend. The λ value for which the resonance is observed depends on the specific coastal slope, as will be illustrated in Section 4.3.

Focusing on the discrepancies for SW simulations we also highlight that: (a) the rupture size for which the resonance is observed is independent of the propagation regime; (b) the overall SW overestimation holds even

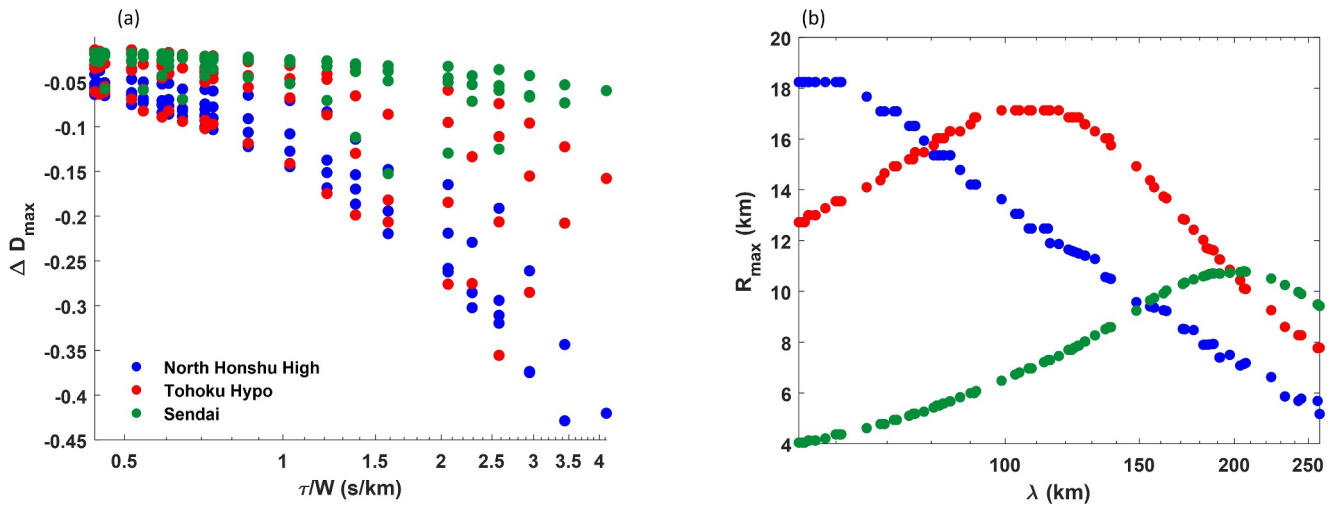


Figure 8. Maximum flow depth and runup for different bathymetric geometry. (a) ΔD_{max} (TD-NH vs. IS-NH) at the first point on the coast for the profiles referred to as “North Honshu High,” “Tohoku Hypo” and “Sendai” respectively according to the map in Figure 1c. (b) Maximum runup R_{max} (for IS-NH case) as a function of horizontal source extension λ for the 3 bathymetric profiles following the same legend of panel (a).

when the more realistic TD-NH and TD-SW are compared. However, in Figure 7d, we observe that while with an IS the SW versus NH ΔR_{max} is always less than 10%, it becomes larger with a TD source, with a maximum of about 16%. Looking at the time evolution of inundation (Figure S15 in Supporting Information S1), we confirm that the largest ΔR_{max} , emerging for small λ in TD simulations, are actually due to the short-wavelength oscillations (left panels of Figure S15 in Supporting Information S1). These oscillations are attenuated for larger ruptures (Figure S15 of Supporting Information S1, right panels) and suppressed for IS simulations (black dotted lines in Figure S14 of Supporting Information S1).

To summarize, as expected in realistic conditions for large subduction earthquakes, where $\lambda \gg H$, with H being the bathymetric depth, the difference between NH and SW models are definitely less significant than the discrepancy emerging between IS and TD simulations, at least in terms of wave maximum amplitude and maximum runup. However, the SW overestimation increases for very slow ruptures leading to $|\Delta| \sim 20\%$ for the investigated metrics. In terms of waveform features, as seen, the use of either a SW model for a TD source or a NH regime for instantaneous seafloor deformation causes short wavelength oscillations affecting both the smaller oscillations behind the primary wave and, sometimes, the inundation metrics, at least for $\lambda < \lambda_R$ with λ_R being the resonance wavelength described in Figure 7c.

4.3. Effect of Bathymetry

To investigate the effect of different bathymetric conditions, particularly as far as the runup resonance is concerned, we repeated the complete set of simulations for the other five simplified topo-bathymetric profiles (Figure 2c). While the six different bathymetries are similar in the deep part, they mostly differ in the slope at shallower depth in the vicinity of the coast and inland. Since some bathymetric profiles are similar, in Figure 8a we only show the results for three of them. The results shown so far were retrieved for the profile referred to as “Tohoku Hypo” (Figure 2c). The southernmost profile referred to as “Sendai” is characterized by a significantly flatter slope, while “North Honshu High” by a steeper slope in the vicinity of the coast. These three profiles are interpreted as a proxy of the overall behavior in presence of intermediate, flat and steep topo-bathymetric profiles, respectively.

Figure 8a shows the $|\Delta D_{max}|$ between IS-NH and TD-NH source simulations at the first point on the coast, for all the simulations and for the 3 different profiles. We retrieve for all the bathymetries the double trend evidenced in Section 4.1 with larger discrepancy emerging not only for slower ruptures but also for large size sources. However, a flatter bathymetry leads to smaller $|\Delta D_{max}|$ implying that when a tsunami wave propagates toward more gentle depth variation an instantaneous source would produce inundation scenarios more similar to time-dependent sources as compared to steeper environments. Contemporarily, in a flatter environment, the

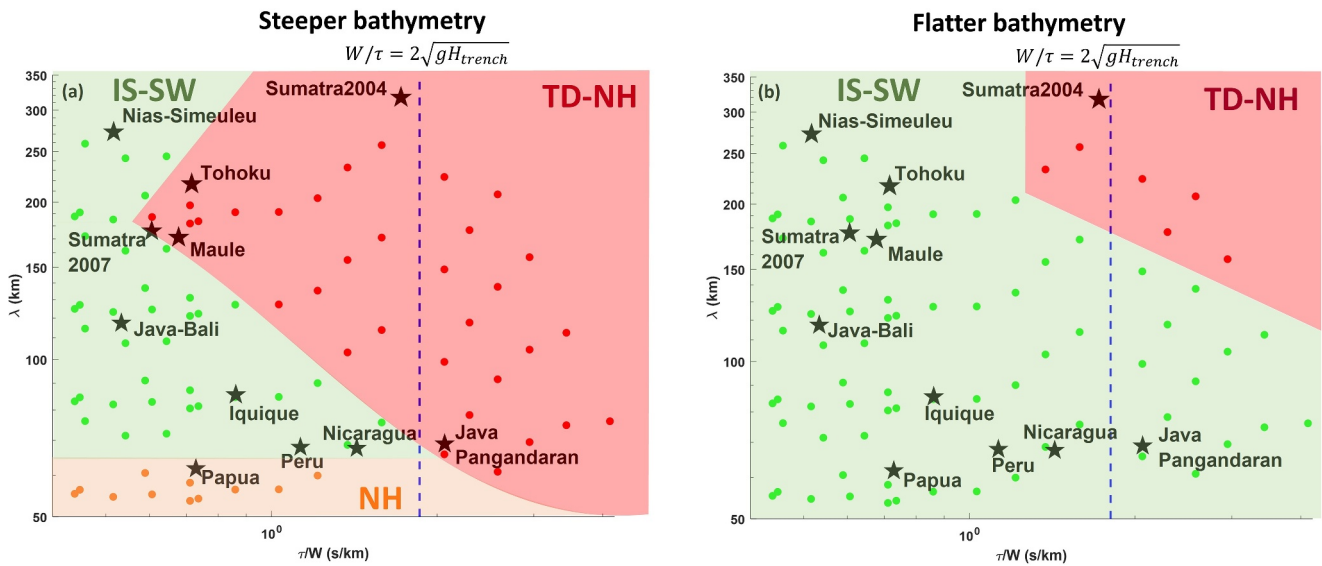


Figure 9. Summary of simulations that can be modeled with (green dots) and without (red and orange dots) enough accuracy using simplified models in terms of maximum runup R . In both panels, each simulation is placed according to τ/W and λ with the green and red dots representing $|\Delta R_{max}| \leq 0.1$ and $|\Delta R_{max}| > 0.1$ respectively when the comparison (TD-NH vs. IS-NH) is performed. Orange dots represent the simulations for which ΔR_{max} (TD-NH vs. IS-NH) < 0.1 while ΔR_{max} (TD-NH vs. TD-SW) > 0.1 . The colored regions indicate the regions where different models must be used. The blue dashed lines border the regions where the seismic rupture velocity proxy W/τ is equal to 2 times the maximum tsunami velocity at the source $\sqrt{gH_{trench}}$. Panels (a) and (b) refer to simulations performed on an intermediate slope (“Tohoku Hypo”) and flat slope bathymetry geometry (“Sendai”), respectively.

inundation is attenuated with smaller flow-depth values on the coast and maximum runup with the size of resonance that increases as the bathymetry slope decreases (see Figure 8b). For the sake of clarity, this latter panel only shows the trends for the IS-NH case. However, we verified that, for all the bathymetries, the rupture size for which the resonance occurs is independent of both the source treatment (IS or TD) and the choice of propagation regime (NH or SW, see also Figure 7c).

In conclusion, a gentler slope of the coast, as in the case of the flood plains in the area of Sendai-Fukushima selects a longer wavelength component of tsunami waves, generating less intense inundations in terms of flow-depth on the coast and smaller maximum runup values. Such a general conclusion that steeper bathymetries generate larger runup might be considered as a specific case of more general runup laws described in Tadepalli and Synolakis (1994). Moreover, in a Tohoku-like environment, like the one we have modeled in this study, the longer wavelengths are more controlled by the deformation occurring very close to the hypocenter (Satake et al., 2013). This contributes to reduce the discrepancy between IS and TD simulations for the flatter bathymetric profiles.

5. Discussion

5.1. Comparison With Real Earthquakes and Tsunamis

To understand in which cases time dependent and/or non-hydrostatic effects should be considered, the 81 simulations performed for the “Tohoku Hypo” bathymetry (intermediate slope) are plotted in Figure 9a as a function of their source duration normalized by size τ/W and horizontal extension λ . They are classified depending on whether the parameter ΔR_{max} (TD-NH vs. IS-NH) is larger (red dots) or smaller (orange and green dots) than 0.1, considering as acceptable a relative discrepancy smaller than 10%. The source duration and size are related to seismic parameters like the stress drop, the average rigidity and hence the average depth of the source (Bilek & Lay, 1999; Geist & Bilek, 2001; Sallarès & Ranero, 2019).

As expected, the slower the rupture the more time-dependent rupture modeling is needed. The instantaneous approximation tends to fail when the characteristic tsunami propagation speed at the source, on the order of $\sqrt{gH_{trench}}$ (with H_{trench} being the depth at the trench) is comparable with the rupture velocity V_r , for which the quantity $(\tau/W)^{-1}$ acts as a proxy (e.g., see Abrahams et al., 2023), as it occurs for the slowest ruptures considered here. However, beyond that, we find that the ΔR_{max} (TD-NH vs. IS-NH) also depends on the source size. Indeed,

larger ruptures, for which along-dip distance is comparable with trench-coast distance, more likely lead to inaccurate solutions from approximated models. In these cases, the inundation is more controlled by what happens at the source rather than by the propagation processes (e.g., the shoaling).

To provide modelers with tangible recommendations, we compared the parameters of the sources presented in Figure 9a with those inferred for some subduction interface tsunamigenic earthquakes. Their features are summarized in Table S3 of Supporting Information S1. We extracted the duration τ , the width W and the dip angle from the teleseismic data inversions by Ye et al. (2016), for all the events, including the Maule 2010 Mw 8.8 and the Tohoku-Oki 2011 Mw 9.1 earthquakes, with the exception of the 2004 Sumatra-Andaman earthquake, whose parameters are taken from the finite-fault model summary released by USGS (https://earthquake.usgs.gov/earthquakes/eventpage/official20041226005853450_30/finite-fault, Banerjee et al., 2007). We computed a proxy of the source size along the dip as $\lambda = W \cdot \cos \delta$, with δ being the dip angle (See Table S3 in Supporting Information S1). Such a comparison in Figure 9 has the goal of comparing the characteristic space and time scales of simulations with those of the real events. However, single real events might be also affected by specific conditions related to local geometry, shallow structure, bathymetry variation, and ratio between source size and trench-coast distance as it happens for the Maule 2010 earthquake (Romano et al., 2020), which may differ from the Tohoku-like setup used in our 1D simulations. Hence, this comparison should be regarded as a general indication. Nonetheless, according to this comparison, some of the megathrust events, characterized by relatively shallow slip and not too high stress-drop, such as Maule 2010 and Tohoku 2011, are very close to the accuracy limit to use an instantaneous source, while the 2004 Sumatra-Andaman event is well in the region where instantaneous source modeling leads to inaccurate solutions and a time-dependent source should be used. The use of a TD source implies, in turn, the necessity of a NH regime to avoid the spurious oscillations shown in Figures S12 and S15 (in Supporting Information S1) and the consequent systematic SW overestimation evidenced in Figures 7c and 7d.

Conversely, large stress drop events (relatively rapid ones, sometimes referred to as “snappy” earthquakes, see e.g. Ebeling & Okal, 2012; Okal et al., 2016) can be well modeled with an instantaneous source. Finally, earthquakes featuring a small extension along the dip, might lead to larger errors when modeled by an instantaneous source, if they are characterized by very slow ruptures, like the tsunami earthquakes (small values of stress drop and rigidity).

However, a direct comparison between the findings of this study and tsunami earthquakes must be interpreted with some prudence, since such events are characterized by a quite large along-strike extension as compared to their width (Kanamori, 1971; Tanioka & Satake, 1996a; Tanioka & Seno, 2001). Such a feature cannot be considered in the 1D model and will be the scope of future work.

Lastly, in Figure 9a the orange dots represent the simulations for which ΔR_{max} (TD-NH vs. IS-NH) < 0.1 while ΔR_{max} (TD-NH vs. TD-SW) > 0.1 . Such simulations are characterized by a small source extension ($\lambda \sim 7H_{trench}$) and, although they could be modeled through an IS description, they require a NH modeling to avoid exceeding the imposed discrepancy tolerance. Within this region we retrieve very short-sized interslab events like the 2009 Papua event or the Tohoku foreshock of 2011, March 9th. In such a case, even if metrics like the maximum runup are accurately modeled through an IS approach, a TD source must be used to prevent the short wavelength oscillations affecting the dispersive secondary waves (See red curves in Figure S14 in Supporting Information S1). For the same reason, for faster events (e.g., deeper, larger stress drop earthquakes for which $\sqrt{gH} \cdot \tau / W \ll 1$), that can be precisely simulated with an IS, the choice of a SW modeling represents a preferable option (see green regions in Figure 9). It is worth to highlight that the acceptable discrepancy threshold between accurate and approximated models depends on the specific applications. For instance when large ensembles of simulations are needed (e.g., for tsunami hazard applications) a large tolerance might be imposed, while for single-scenario applications (e.g., for source inversions forward modeling) it might be convenient to impose a smaller threshold. However, although a threshold fixed at 10% is here purely illustrative, the general results just discussed hold regardless this choice.

We have verified that ΔD_{max} or ΔR_{max} depend also on topographic features (see Figure 8a). Figure 9b shows the same plot as Figure 9a with the ΔR_{max} values, but using the flatter “Sendai” near-coast bathymetry and topography. As shown in Figure 8a, the ΔD_{max} values on the coast are smaller for flatter bathymetries and this leads to smaller Δ values also in terms of maximum runup. As a consequence, only very slow ($V_r < 0.5$ km/s) and large ruptures (λ larger than half trench-coast distance) yield inaccurate inundation modeling when an IS source is used

as a tsunami generation mechanism. Only the modeling of events similar to the giant 2004 Sumatra-Andaman event would require a TD source. The differences highlighted between Figures 9a and b are consistent with the results related to the 2011 Tohoku-Oki event, by Satake et al. (2013) who showed how a time-dependent source modeling is required to accurately retrieve the inundation features along the coast in front of the hypocenter of the event. Satake et al. (2013) also showed that an instantaneous source was enough to model a realistic inundation in the southern regions of Sendai and Fukushima. For flatter bathymetries, for which the shortest wavelength sources generate negligible inundations, all the ΔR_{max} (TD-NH-vs TD-SW) values are below the imposed tolerance of 0.1. For the sake of completeness, the results summarized in Figure 9 are compared with the condition $W/\tau = 2\sqrt{gH_{trench}}$ that represents a proxy of the instantaneous source limit (Abrahams et al., 2023). An equivalent horizontal line fixing as a reference a SW limit $\lambda = 2H_{trench}$ would be well below the shortest modeled source.

At least for a Tohoku-like up-dip rupture, using an instantaneous source always overestimates the inundation on the coast as compared to the corresponding time dependent modeling. Therefore, for some applications, the IS can be still used as a conservative approach, even though relatively inaccurate, if a kinematic or a dynamic realistic description of the seismic source process is not available. Nevertheless, we have also verified that for some simulations the maximum amplitude of waves propagating toward the open ocean along the directive direction is underestimated by the IS modeling. This might produce an underestimated inundation warning toward those islands which are located along the up-dip direction, in the vicinity of the trench.

5.2. Resonant Maximum Runup Amplification

Another important result concerns the resonant amplification of the maximum runup observed for specific source sizes (see Figures 7c and 8b) and its connection to the geometry of bathymetric profiles. In this framework, Stefanakis et al. (2012) have shown how a monochromatic source, with pulsation ω , generates resonant waves whose maximum runup on planar beaches depends on the incident wavelength and beach slope (with larger runups associated with steeper slopes). They verified that for a fixed beach length L the resonance is always retrieved at the same normalized pulsation $\omega' = \omega/\sqrt{g \tan \theta/L}$, with g and θ being the gravity acceleration and the slope of the bathymetry (in the vicinity of the beach and inland), respectively. To verify the consistency of the same model for our application, we can replace ω with $1/\lambda$ since in the vicinity of the source the depth variation and hence the propagation velocity are the same for all the bathymetries. Moreover, we can neglect the effect of L because the beaches are always long enough to avoid backward reflections. Figure 10 shows the maximum runup R_{max} for all the 81 IS-NH simulations and the 6 bathymetries, as a function of the parameter $1/(\lambda\sqrt{\tan \theta})$, θ being the different slopes of the bathymetry in the vicinity and on the coast. Although the sources modeled in this work are quite different as compared to the simplified monochromatic source, with characteristic wavelength inherited by a realistic parameterization of the seismic rupture, the resonant mechanism is preserved (compare Figure 10 with Figure 8c) at least for instantaneous sources. When a TD source is implemented this resonance symmetry is partially smeared since the maximum runup is also controlled by the seismic source duration (See Figure 7c), with slower ruptures leading to smaller inundation. This latter result challenges the common assumption, for example, for tsunami earthquakes, that slow ruptures are one of the reasons why larger than expected tsunami inundation for a given earthquake magnitude is observed. Nevertheless, our modeling indicates that the inundation amplification could still be due to larger slip occurring at shallower depths, where the surrounding medium is weaker, and/or eventually to an unexpectedly large extension of the rupture along the strike direction.

5.3. Limits of Numerical Modeling

Some of the choices made in terms of seismic source parameters deserve further discussion since they can affect the investigated tsunami metrics. As an example, different values of the critical slip weakening distance D_c or the possibility to consider the contribution of horizontal sea-floor deformation (Tanioka & Satake, 1996b; Tanioka & Seno, 2001) to the tsunami initial condition might modify the maximum amplitude of the tsunami source (see Figure 2b) and hence generate different wave amplitudes, flow-depths, and maximum runups. Besides, as discussed in Sections 2 and 3, we used a single slope to model the interface between the fault and the seafloor for all the cases and this allowed us to perform several tsunami simulations from a single rupture dynamic simulation. However, the use of a different and more realistic interface geometry is expected to slightly change the wave amplitudes as an effect of the variable dip and its time history, even when ending up with the same residual amplitude (See Figure S16a in Supporting Information S1). Nevertheless, at least regarding the latter point, we

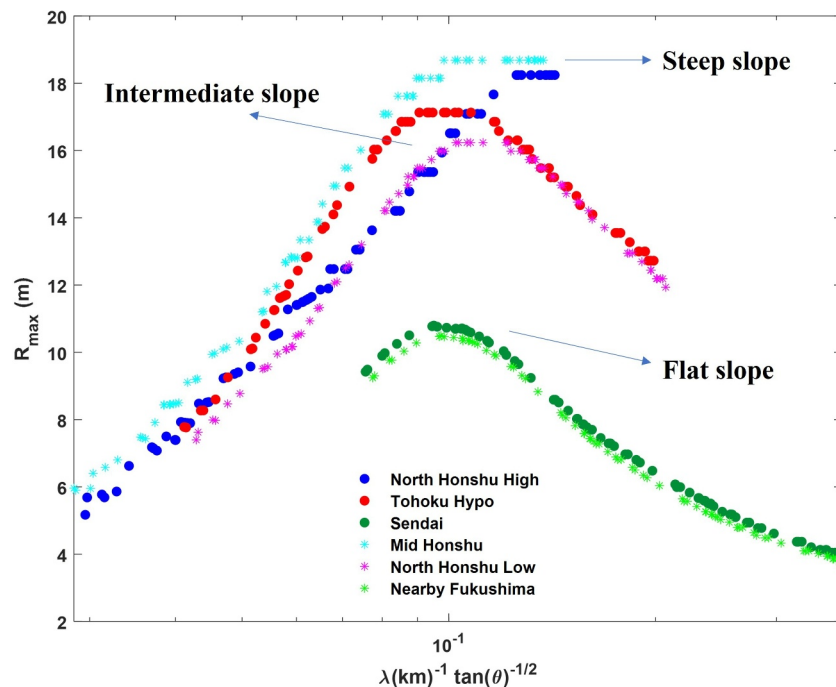


Figure 10. Maximum runup as a function of $1/(\lambda\sqrt{\tan\theta})$ as suggested by the model of Stefanakis et al. (2012). As indicated by the arrows the blue dots and cyan stars refer to steeper slope geometry, the red dots and magenta stars to intermediate slope and the dark green dots and green stars to flatter slope bathymetry, respectively, as indicated in the legend.

verified for some of the performed simulations that the ranges of ΔD_{max} on the coast and the $\Delta\eta_{max}$ offshore values (for TD-NH vs. IS-NH comparison) are not significantly affected by these initial source perturbations (See Figure S16 and its caption in Supporting Information S1). Therefore, we can argue that the results presented in Section 4 as well as the general interpretation presented in this section hold for most of the conditions that simply affect the maximum amplitude of the waves triggered in the vicinity of the source.

We focused on megathrust earthquakes while tsunamis may arise also from other type of mechanisms such as the outer-rise normal events for which time-dependent and non-hydrostatic modeling might have a non-negligible effect as well (Baba et al., 2021). One should be cautious to extend the findings of this study to those events and related tsunamis because they feature different radiation fields and sea-floor deformation history and space scale.

The simulations were performed with a simplified geometrical description of earthquake rupture and tsunami and a linear slip weakening friction law. More complex rupture dynamic models, tailored for specific cases, might affect the results. Indeed, different constitutive laws (e.g., rate and state Ruina, 1983), incorporating physical processes in competition with friction (e.g., thermal weakening Di Toro et al., 2011; Murphy et al., 2018; Ulrich et al., 2022) or energy dissipation in the fault zone (e.g., off-fault damage, Thomas & Bhat, 2018; Wilson & Ma, 2021; Ma, 2023) could reduce the high-frequency content of the radiation and modify the characteristic space and time scales of the tsunami initial conditions. Similarly, a fault embedded in a inhomogeneous medium, possibly separating layers with different elastic properties, and reaching low velocity accretionary wedges, would be characterized by a different rupture velocity and longer duration, due to the bimaterial effect (e.g., Scala et al., 2017) and amplification of trapped waves in the shallow layers (Ma & Hirakawa, 2013).

Moreover, the rupture variability is modeled only along the dip direction. To account for the rupture length along the strike direction and provide an estimate of earthquake magnitude, we used the scaling relationship of Strasser et al. (2010). The use of other relationships, also calibrated for subduction earthquakes (Leonard, 2010; Murotani et al., 2013), would increase the range of characteristic widths for the same seismic moment, but not affect the selection of the optimal strategy for tsunami modeling.

The use of very simple bathymetric profiles is aimed to assess to what extent the slope of the bathymetry affects the tsunami waves for all the source and propagation models. In this sense, the use of a case-specific bathymetry, that incorporates small scale variations, might affect the results due to specific local conditions. A general sensitivity of different models to such short-scale bathymetric features is well beyond the scope of this work. However, to verify that a sharp variation in the bathymetry slope does not introduce a singularity in the propagation, we compared our results with the ones obtained with a smoother version of the “Tohoku-hypo” bathymetry (see Figure S17 in Supporting Information S1). The results, summarized in Movies S11 and S12 in Supporting Information for a large and a small rupture model respectively, confirm that the tsunami investigated metrics are unmodified, despite small differences in tsunami wave velocity.

Finally, we are aware that moving toward a fully 2D rupture in a heterogeneous medium, is necessary to catch specific effects due to the variability of the along-strike earthquake source and bathymetry. These effects couple spatial and temporal scales along the two directions and deserve a deeper investigation in a 3D coupled seismic-tsunami source and propagation model. Such a fully coupled model will also allow to assess the best modeling strategy to simultaneously take into account the propagation effects here described (i.e., the transversal propagation of dispersive waves and the maximum runup resonant amplification on the continental shelf) and the characteristic longshore processes, like the amplification of trapping waves due the concave shape of the bay (Kim et al., 2016) and the edge waves propagation (Geist, 2016; Koyano et al., 2021). Nevertheless, we believe that the results here presented already provide crucial hints for the tsunami modelers community for a direct use in practical applications.

6. Conclusions

The main goal of this work is to understand when the accuracy needed to model the earthquake source and tsunami generation can be achieved with the commonly adopted simplifications (e.g., instantaneous source, shallow water) and when more sophisticated modeling strategies are necessary. This might be relevant for a broad range of applications in tsunami science like the PTHA (e.g., Basili et al., 2021; Behrens et al., 2021; Davies et al., 2018; Grezio et al., 2017), where many scenarios need to be simulated, and tsunami early warning (e.g., Selva et al., 2021), where a short time-to-solution is needed, as well as for other applications (e.g., tsunami source inversions Satake et al., 2013; Romano et al., 2021). We measured the accuracy of the solutions in terms of wave amplitude and metrics like the flow-depth and maximum runup for a Tohoku-like test-case using different topo-bathymetric morphologies. We systematically compared the approximated results and the ones deriving from a more realistic representation of the physical processes, accounting for a time-dependent earthquake-tsunami source and/or a multi-layer non-hydrostatic tsunami modeling. We varied systematically the duration and the size of the tsunami sources, using realistic ranges related to the corresponding seismic source and surrounding medium parameters, in particular the stress drop and the rigidity around the fault plane.

The main results can be summarized as follows:

1. An instantaneous source leads to increasingly less accurate results as the velocity of the seismic source decreases and becomes comparable with the characteristic velocity of tsunami propagation, in turn proportional to the square root of the bathymetric depth. However, within this framework, the size of the rupture also plays a fundamental role with larger ruptures leading to less accurate solutions. The inundation metrics are systematically overestimated by the instantaneous source approximation.
2. For what concerns the comparison between shallow water and non-hydrostatic, in realistic conditions featuring an average bathymetric depth $H \ll \lambda$ (horizontal extent of the source) the discrepancy for the maximum wave amplitudes and inundations are often not significant. Even for very small ruptures the relative flow-depth and runup overestimation from SW-IS as compared to NH-IS are always smaller than 10%. Nevertheless, when we compare NH and SW in those conditions requiring TD source modeling, such discrepancy increases up to ~20%. Thus, it is almost always recommended to use NH modeling when dealing with time dependent seismic ruptures. In this frame, the common use of multi sub-faults, activated at different instants, along with a SW propagation, might lead to large overestimation.
3. All the presented results depend on the geometric characteristics of the topo/bathymetry in the vicinity of the coast and inland. The differences between TD and IS inundation on flatter bathymetric profiles (e.g., the ones characterizing the flood plains) are smaller than those for steeper profiles. As a result, flooding on a flatter

- bathymetry could be modeled with sufficient accuracy as an instantaneous source, as has been shown for some real tsunamigenic events (Satake et al., 2013).
- The maximum runup features a resonant mechanism that is an amplified R_{max} in correspondence of a narrow range of the source size λ . The size of resonance was shown to be inversely proportional to $\sqrt{\tan \theta}$ with θ being the topo-bathymetry slope in the vicinity of the coastline.
 - Comparing all these results with real events, we found that megathrust and tsunami earthquakes might require non-hydrostatic time-dependent modeling, in particular for more pronounced variation of nearshore topo-bathymetry to prevent overestimation of inundation intensity. Conversely, tsunami generated by deeper higher stress drop seismic ruptures can be simulated through approximated IS-SW modeling, still preserving enough accuracy in terms of propagating waves and inundation features.

Data Availability Statement

The whole simulated data set is available at Scala (2024). All the figures were originally produced for this paper through the software MATLAB: version 2023b. First accessed: September 2023. Academic license number: 40500131.

Acknowledgments

This research has been partially funded by MCIN/AEI/10.13039/501100011033 and by the “European Union NextGenerationEU/PRTR” through the Grant PDC2022-133663-C21 and by MCIN/AEI/10.13039/501100011033 and by “ERDF A way of making Europe,” by the European Union through the Grant PID2022-137637NB-C21, by the HORIZON EUROPE Framework Programme through the Grants 101058518 (AS and GF) and 101058129 (SL, FR, AA, HBB, MJCD and JM). AA was also supported by a research scholarship from the PhD program “Earth Science, Fluid-dynamics and Mathematics” co-funded by INGV and Università di Trieste, Italy, while CES, MJCD and JM were also partially supported by the European High Performance Computing Joint Undertaking through the Grant 101093038. The authors thank the two reviewers and the editor for the valuable comments that have improved the quality of the paper. Open access publishing facilitated by Università degli Studi di Napoli Federico II, as part of the Wiley - CRUI-CARE agreement.

References

- Abbate, A., González Vida, J. M., Castro Díaz, M. J., Romano, F., Bayraktar, H. B., Babeyko, A., & Lorito, S. (2024). Modelling tsunami initial conditions due to rapid coseismic seafloor displacement: Efficient numerical integration and a tool to build unit source databases. *Natural Hazards and Earth System Sciences*, 24, 2773–2791. <https://doi.org/10.5194/nhess-24-2773-2024>
- Abercrombie, R. E., Bannister, S., Ristau, J., & Doser, D. (2017). Variability of earthquake stress drop in a subduction setting, the Hikurangi Margin, New Zealand. *Geophysical Journal International*, 208(1), 306–320. <https://doi.org/10.1093/gji/ggw393>
- Abrahams, L. S., Krenz, L., Dunham, E. M., Gabriel, A.-A., & Saito, T. (2023). Comparison of methods for coupled earthquake and tsunami modelling. *Geophysical Journal International*, 234(1), 404–426. <https://doi.org/10.1093/gji/ggad053>
- Audusse, E., Bristeau, M.-O., Perthame, B., & Sainte-Marie, J. (2011). A multilayer Saint-Venant system with mass exchanges for shallow water flows. Derivation and numerical validation. *ESAIM: Mathematical Modelling and Numerical Analysis*, 45(1), 169–200. <https://doi.org/10.1051/m2an/2010036>
- Baba, T., Chikasada, N., Imai, K., Tanioka, Y., & Kodaira, S. (2021). Frequency dispersion amplifies tsunamis caused by outer-rise normal faults. *Scientific Reports*, 11(1), 20064. <https://doi.org/10.1038/s41598-021-99536-x>
- Babeyko, A., Lorito, S., Hernandez, F., Lauterjung, J., Løvholt, F., Rudloff, A., et al. (2022). Towards the new thematic core service tsunami within the EPOS research infrastructure. *Annals of Geophysics*, 65(2), DM215. <https://doi.org/10.4401/ag-8762>
- Banerjee, P., Pollitz, F., Nagarajan, B., & Burgmann, R. (2007). Coseismic slip distributions of the 26 December 2004 Sumatra–Andaman and 28 March 2005 Nias earthquakes from GPS static offsets. *Bulletin of the Seismological Society of America*, 97(1A), S86–S102. <https://doi.org/10.1785/0120050609>
- Basili, R., Brizuela, B., Herrero, A., Iqbal, S., Lorito, S., Maesano, F. E., et al. (2021). The making of the NEAM tsunami hazard model 2018 (NEAMTHM18). *Frontiers in Earth Science*, 8. <https://doi.org/10.3389/feart.2020.616594>
- Behrens, J., Løvholt, F., Jalayer, F., Lorito, S., Salgado-Gálvez, M. A., Sørensen, M., et al. (2021). Probabilistic tsunami hazard and risk analysis: A review of research gaps. *Frontiers in Earth Science*, 9, 628772. <https://doi.org/10.3389/feart.2021.628772>
- Bilek, S. L., & Lay, T. (1999). Rigidity variations with depth along interplate megathrust faults in subduction zones. *Nature*, 400(6743), 443–446. <https://doi.org/10.1038/22739>
- Bilek, S. L., Rotman, H. M. M., & Phillips, W. S. (2016). Low stress drop earthquakes in the rupture zone of the 1992 Nicaragua tsunami earthquake. *Geophysical Research Letters*, 43(19), 10–180. <https://doi.org/10.1002/2016GL070409>
- Bizzarri, A., & Cocco, M. (2003). Slip-weakening behavior during the propagation of dynamic ruptures obeying rate- and state-dependent friction laws. *Journal of Geophysical Research*, 108(B8). <https://doi.org/10.1029/2002JB002198>
- Bonaventura, L., Fernández-Nieto, E. D., Garres-Díaz, J., & Narbona-Reina, G. (2018). Multilayer shallow water models with locally variable number of layers and semi-implicit time discretization. *Journal of Computational Physics*, 364, 209–234. <https://doi.org/10.1016/j.jcp.2018.03.017>
- Brocchini, M., & Peregrine, D. H. (1996). Integral flow properties of the swash zone and averaging. *Journal of Fluid Mechanics*, 317, 241–273. <https://doi.org/10.1017/S0022112096000742>
- Burridge, R. (1973). Admissible speeds for plane-strain self-similar shear cracks with friction but lacking cohesion. *Geophysical Journal International*, 35(4), 439–455. <https://doi.org/10.1111/j.1365-246X.1973.tb00608.x>
- Casulli, V. (1999). A semi-implicit finite difference method for non-hydrostatic, free-surface flows. *International Journal for Numerical Methods in Fluids*, 30(4), 425–440. [https://doi.org/10.1002/\(SICI\)1097-0363\(19990630\)30:4<425::AID-FLD847>3.0.CO;2-D](https://doi.org/10.1002/(SICI)1097-0363(19990630)30:4<425::AID-FLD847>3.0.CO;2-D)
- Davies, G., & Griffin, J. (2020). Sensitivity of probabilistic tsunami hazard assessment to far-field earthquake slip complexity and rigidity depth-dependence: Case study of Australia. *Pure and Applied Geophysics*, 177(3), 1521–1548. <https://doi.org/10.1007/s00024-019-02299-w>
- Davies, G., Griffin, J., Løvholt, F., Glimsdal, S., Harbitz, C., Thio, H. K., et al. (2018). A global probabilistic tsunami hazard assessment from earthquake sources. *Geological Society, London, Special Publications*, 456(1), 219–244. <https://doi.org/10.1144/SP456.5>
- Di Toro, G., Han, R., Hirose, T., De Paola, N., Nielsen, S., Mizoguchi, K., et al. (2011). Fault lubrication during earthquakes. *Nature*, 471(7339), 494–498. <https://doi.org/10.1038/nature09838>
- Earthquake Research Committee, The Headquarters for Earthquake Research Promotion. (2017). Procedures to build a subsurface velocity structure model. Retrieved from https://www.jishin.go.jp/main/chousa/17apr_chikakozo/model_concept-e.pdf
- Ebeling, C. W., & Okal, E. A. (2012). An extension of the E/M0 tsunami earthquake discriminant Θ to regional distances. *Geophysical Journal International*, 190(3), 1640–1656. <https://doi.org/10.1111/j.1365-246X.2012.05566.x>
- Ehara, A., Salmanidou, D. M., Heidarzadeh, M., & Guillias, S. (2023). Multi-level emulation of tsunami simulations over Cilacap, South Java, Indonesia. *Computational Geosciences*, 27(1), 127–142. <https://doi.org/10.1007/s10596-022-10183-1>

- Escalante, C., Fernández-Nieto, E. D., Garres-Díaz, J., & Mangeney, A. (2023a). Multilayer shallow model for dry granular flows with a weakly non-hydrostatic pressure. *Journal of Scientific Computing*, 96(3), 88. <https://doi.org/10.1007/s10915-023-02299-y>
- Escalante, C., Fernández-Nieto, E. D., Garres-Díaz, J., Morales de Luna, T., & Penel, Y. (2023b). Non-hydrostatic layer-averaged approximation of Euler system with enhanced dispersion properties. *Computational and Applied Mathematics*, 42(4), 177. <https://doi.org/10.1007/s40314-023-02309-7>
- Escalante, C., Fernández-Nieto, E. D., Morales de Luna, T., & Castro, M. J. (2019). An efficient two-layer non-hydrostatic approach for dispersive water waves. *Journal of Scientific Computing*, 79(1), 273–320. <https://doi.org/10.1007/s10915-018-0849-9>
- Escalante, C., Morales de Luna, T., & Castro, M. J. (2018). Non-hydrostatic pressure shallow flows: GPU implementation using finite volume and finite difference scheme. *Applied Mathematics and Computation*, 338, 631–659. <https://doi.org/10.1016/j.amc.2018.06.035>
- Fernández-Nieto, E. D., Koné, E. H., & Chacón Rebollo, T. (2014). A multilayer method for the hydrostatic Navier-Stokes equations: A particular weak solution. *Journal of Scientific Computing*, 60(2), 408–437. <https://doi.org/10.1007/s10915-013-9802-0>
- Fernández-Nieto, E. D., Parisot, M., Penel, Y., & Sainte-Marie, J. (2018). A hierarchy of dispersive layer-averaged approximations of Euler equations for free surface flows. *Communications in Mathematical Sciences*, 16(5), 1169–1202. <https://doi.org/10.4310/CMS.2018.v16.n5.a1>
- Festa, G., & Vilotte, J.-P. (2005). The Newmark scheme as velocity-stress time-staggering: An efficient PML implementation for spectral element simulations of elastodynamics. *Geophysical Journal International*, 161(3), 789–812. <https://doi.org/10.1111/j.1365-246X.2005.02601.x>
- Folesky, J., Kummerow, J., & Shapiro, S. A. (2021). Stress drop variations in the region of the 2014 M W 8.1 Iquique earthquake, Northern Chile. *Journal of Geophysical Research: Solid Earth*, 126(4). <https://doi.org/10.1029/2020JB020112>
- Gailler, A., Hébert, H., Schindelé, F., & Reymond, D. (2018). Coastal amplification laws for the French tsunami warning center: Numerical modeling and fast estimate of tsunami wave heights along the French Riviera. *Pure and Applied Geophysics*, 175(4), 1429–1444. <https://doi.org/10.1007/s00024-017-1713-9>
- Geist, E. L. (2016). Non-linear resonant coupling of tsunami edge waves using stochastic earthquake source models. *Geophysical Journal International*, 204(2), 878–891. <https://doi.org/10.1093/gji/ggv489>
- Geist, E. L., & Bilek, S. L. (2001). Effect of depth-dependent shear modulus on tsunami generation along subduction zones. *Geophysical Research Letters*, 28(7), 1315–1318. <https://doi.org/10.1029/2000GL012385>
- Gibbons, S. J., Lorito, S., Macías, J., Løvholt, F., Selva, J., Volpe, M., et al. (2020). Probabilistic tsunami hazard analysis: High performance computing for massive scale inundation simulations. *Frontiers in Earth Science*, 8, 591549. <https://doi.org/10.3389/feart.2020.591549>
- Glimsdal, S., Løvholt, F., Harbitz, C. B., Romano, F., Lorito, S., Orefice, S., et al. (2019). A new approximate method for quantifying tsunami maximum inundation height probability. *Pure and Applied Geophysics*, 176(7), 3227–3246. <https://doi.org/10.1007/s00024-019-02091-w>
- Gopinathan, D., Heidarzadeh, M., & Guillas, S. (2021). Probabilistic quantification of tsunami current hazard using statistical emulation. *Proceedings of the Royal Society A: Mathematical, Physical and Engineering Sciences*, 477(2250), 20210180. <https://doi.org/10.1098/rspa.2021.0180>
- Grezio, A., Babeyko, A., Baptista, M. A., Behrens, J., Costa, A., Davies, G., et al. (2017). Probabilistic tsunami hazard analysis: Multiple sources and global applications. *Reviews of Geophysics*, 55(4), 1158–1198. <https://doi.org/10.1002/2017RG000579>
- Hayes, G. P., Moore, G. L., Portner, D. E., Hearne, M., Flamme, H., Furtney, M., & Smoczyk, G. M. (2018). Slab2, a comprehensive subduction zone geometry model. *Science*, 362(6410), 58–61. <https://doi.org/10.1126/science.aat4723>
- Huang, Y., Meng, L., & Ampuero, J.-P. (2012). A dynamic model of the frequency-dependent rupture process of the 2011 Tohoku-Oki earthquake. *Earth Planets and Space*, 64(12), 1061–1066. <https://doi.org/10.5047/eps.2012.05.011>
- Ida, Y. (1972). Cohesive force across the tip of a longitudinal-shear crack and Griffith's specific surface energy. *Journal of Geophysical Research*, 77(20), 3796–3805. <https://doi.org/10.1029/JB077i020p03796>
- Kajitara, K. (1963). *The leading wave of a tsunami* (Vol. 41, pp. 535–571). Bulletin of Earthquake Research Institute, University of Tokyo.
- Kanamori, H. (1971). Seismological evidence for a lithospheric normal faulting — The Sanriku earthquake of 1933. *Physics of the Earth and Planetary Interiors*, 4(4), 289–300. [https://doi.org/10.1016/0031-9201\(71\)90013-6](https://doi.org/10.1016/0031-9201(71)90013-6)
- Kanamori, H., & Brodsky, E. E. (2004). The physics of earthquakes. *Reports on Progress in Physics*, 67(8), 1429–1496. <https://doi.org/10.1088/0034-4885/67/8/R03>
- Kim, G. H., Jin, S., Hyun, S. G., & Yoon, S. B. (2016). Resonance of 2011 East Japan tsunami over continental shelf along Ibaraki coast of Japan. *Journal of Coastal Research*, 75(sp1), 1137–1141. <https://doi.org/10.2112/S175-228.1>
- Komatitsch, D., & Vilotte, J.-P. (1998). The spectral element method: An efficient tool to simulate the seismic response of 2D and 3D geological structures. *Bulletin of the Seismological Society of America*, 88(2), 368–392. <https://doi.org/10.1785/BSSA0880020368>
- Koyano, K., Takabatake, T., Esteban, M., & Shibayama, T. (2021). Influence of edge waves on tsunami characteristics along Kujukuri beach, Japan. *Journal of Waterway, Port, Coastal, and Ocean Engineering*, 147(1). [https://doi.org/10.1061/\(ASCE\)WW.1943-5460.0000617](https://doi.org/10.1061/(ASCE)WW.1943-5460.0000617)
- Kozdon, J. E., & Dunham, E. M. (2013). Rupture to the trench: Dynamic rupture simulations of the 11 March 2011 Tohoku earthquake. *Bulletin of the Seismological Society of America*, 103(2B), 1275–1289. <https://doi.org/10.1785/0120120136>
- Krenz, L., Uphoff, C., Ulrich, T., Gabriel, A.-A., Abrahams, L. S., Dunham, E. M., & Bader, M. (2021). 3D acoustic-elastic coupling with gravity. In *Proceedings of the International Conference for High Performance Computing, Networking, Storage and Analysis* (pp. 1–14). <https://doi.org/10.1145/3458817.3476173>
- Leonard, M. (2010). Earthquake Fault scaling: Self-consistent relating of rupture length, width, average displacement, and moment release. *Bulletin of the Seismological Society of America*, 100(5A), 1971–1988. <https://doi.org/10.1785/0120090189>
- LeVeque, R. J., Waagan, K., González, F. I., Rim, D., & Lin, G. (2016). Generating random earthquake events for probabilistic tsunami hazard assessment. *Pure and Applied Geophysics*, 173(12), 3671–3692. <https://doi.org/10.1007/s00024-016-1357-1>
- Li, L., Lay, T., Cheung, K. F., & Ye, L. (2016). Joint modeling of teleseismic and tsunami wave observations to constrain the 16 September 2015 Illapel, Chile, M w 8.3 earthquake rupture process. *Geophysical Research Letters*, 43(9), 4303–4312. <https://doi.org/10.1002/2016GL068674>
- Lotto, G. C., & Dunham, E. M. (2015). High-order finite difference modeling of tsunami generation in a compressible ocean from offshore earthquakes. *Computational Geosciences*, 19(2), 327–340. <https://doi.org/10.1007/s10596-015-9472-0>
- Lotto, G. C., Jeppson, T. N., & Dunham, E. M. (2019). Fully coupled simulations of megathrust earthquakes and tsunamis in the Japan trench, Nankai trough, and Cascadia subduction zone. *Pure and Applied Geophysics*, 176(9), 4009–4041. <https://doi.org/10.1007/s00024-018-1990-y>
- Ludwig, W. J., Nafe, J. E., & Drake, C. L. (1970). Seismic refraction New York: Wiley-Interscience. In A. E. Maxwell (Ed.), *The Sea* (Vol. 4(1), pp. 53–84).
- Ma, G., Shi, F., & Kirby, J. T. (2012). Shock-capturing non-hydrostatic model for fully dispersive surface wave processes. *Ocean Modelling*, 43–44, 22–35. <https://doi.org/10.1016/j.ocemod.2011.12.002>
- Ma, S. (2023). Wedge plasticity and a minimalist dynamic rupture model for the 2011 MW 9.1 Tohoku-Oki earthquake and tsunami. *Tectonophysics*, 869, 230146. <https://doi.org/10.1016/j.tecto.2023.230146>

- Ma, S., & Hirakawa, E. T. (2013). Dynamic wedge failure reveals anomalous energy radiation of shallow subduction earthquakes. *Earth and Planetary Science Letters*, 375, 113–122. <https://doi.org/10.1016/j.epsl.2013.05.016>
- Macías, J., Escalante, C., & Castro, M. J. (2021a). Multilayer-HySEA model validation for landslide-generated tsunamis – Part 1: Rigid slides. *Natural Hazards and Earth System Sciences*, 21(2), 775–789. <https://doi.org/10.5194/nhess-21-775-2021>
- Macías, J., Escalante, C., & Castro, M. J. (2021b). Multilayer-HySEA model validation for landslide-generated tsunamis – Part 2: Granular slides. *Natural Hazards and Earth System Sciences*, 21(2), 791–805. <https://doi.org/10.5194/nhess-21-791-2021>
- Madden, E. H., Bader, M., Behrens, J., van Dinther, Y., Gabriel, A.-A., Rannabauer, L., et al. (2020). Linked 3-D modelling of megathrust earthquake-tsunami events: From subduction to tsunami run up. *Geophysical Journal International*, 224(1), 487–516. <https://doi.org/10.1093/gji/ggaa484>
- Makinoshima, F., Oishi, Y., Yamazaki, T., Furumura, T., & Imamura, F. (2021). Early forecasting of tsunami inundation from tsunami and geodetic observation data with convolutional neural networks. *Nature Communications*, 12(1), 2253. <https://doi.org/10.1038/s41467-021-22348-0>
- Meade, B. J. (2007). Algorithms for the calculation of exact displacements, strains, and stresses for triangular dislocation elements in a uniform elastic half space. *Computers and Geosciences*, 33(8), 1064–1075. <https://doi.org/10.1016/j.cageo.2006.12.003>
- Miyake, H., Koketsu, K., & Furumura, T. (2008). Source modeling of subduction-zone earthquakes and long-period ground motion validation in the Tokyo metropolitan area.
- Murotani, S., Satake, K., & Fujii, Y. (2013). Scaling relations of seismic moment, rupture area, average slip, and asperity size for $M \sim 9$ subduction-zone earthquakes. *Geophysical Research Letters*, 40(19), 5070–5074. <https://doi.org/10.1002/grl.50976>
- Murphy, S., Di Toro, G., Romano, F., Scala, A., Lorito, S., Spagnuolo, E., et al. (2018). Tsunamiogenic earthquake simulations using experimentally derived friction laws. *Earth and Planetary Science Letters*, 486, 155–165. <https://doi.org/10.1016/j.epsl.2018.01.011>
- Murphy, S., Scala, A., Herrero, A., Lorito, S., Festa, G., Trasatti, E., et al. (2016). Shallow slip amplification and enhanced tsunami hazard unravelled by dynamic simulations of mega-thrust earthquakes. *Scientific Reports*, 6(1), 35007. <https://doi.org/10.1038/srep35007>
- Nakano, M., Murphy, S., Agata, R., Igarashi, Y., Okada, M., & Hori, T. (2020). Self-similar stochastic slip distributions on a non-planar fault for tsunami scenarios for megathrust earthquakes. *Progress in Earth and Planetary Science*, 7(1), 45. <https://doi.org/10.1186/s40645-020-00360-0>
- Oglesby, D. D., Archuleta, R. J., & Nielsen, S. B. (2000). Dynamics of dip-slip faulting: Explorations in two dimensions. *Journal of Geophysical Research*, 105(B6), 13643–13653. <https://doi.org/10.1029/2000JB900055>
- Okada, Y. (1985). Surface deformation due to shear and tensile faults in a half-space. *Bulletin of the Seismological Society of America*, 75(4), 1135–1154. <https://doi.org/10.1785/BSSA0750041135>
- Okal, E. A., Kirby, S. H., & Kalligeris, N. (2016). The Showa Sanriku earthquake of 1933 March 2: A global seismological reassessment. *Geophysical Journal International*, 206(3), 1492–1514. <https://doi.org/10.1093/gji/ggw206>
- Polet, J., & Kanamori, H. (2000). Shallow subduction zone earthquakes and their tsunamiogenic potential. *Geophysical Journal International*, 142(3), 684–702. <https://doi.org/10.1046/j.1365-246x.2000.00205.x>
- Roerber, V., Cheung, K. F., & Kobayashi, M. H. (2010). Shock-capturing Boussinesq-type model for nearshore wave processes. *Coastal Engineering*, 57(4), 407–423. <https://doi.org/10.1016/j.coastaleng.2009.11.007>
- Romano, F., Gusman, A. R., Power, W., Piatanesi, A., Volpe, M., Scala, A., & Lorito, S. (2021). Tsunami source of the 2021 M W 8.1 Raoul island earthquake from DART and tide-gauge data inversion. *Geophysical Research Letters*, 48(17), e2021GL094449. <https://doi.org/10.1029/2021GL094449>
- Romano, F., Lorito, S., Lay, T., Piatanesi, A., Volpe, M., Murphy, S., & Tonini, R. (2020). Benchmarking the optimal time alignment of tsunami waveforms in nonlinear joint inversions for the Mw 8.8 2010 Maule (Chile) earthquake. *Frontiers in Earth Science*, 8, 585429. <https://doi.org/10.3389/feart.2020.585429>
- Ruina, A. (1983). Slip instability and state variable friction laws. *Journal of Geophysical Research*, 88(B12), 10359–10370. <https://doi.org/10.1029/JB088iB12p10359>
- Saito, T., Baba, T., Inazu, D., Takemura, S., & Fukuyama, E. (2019). Synthesizing sea surface height change including seismic waves and tsunami using a dynamic rupture scenario of anticipated Nankai trough earthquakes. *Tectonophysics*, 769, 228166. <https://doi.org/10.1016/j.tecto.2019.228166>
- Sallarès, V., & Ranero, C. R. (2019). Upper-plate rigidity determines depth-varying rupture behaviour of megathrust earthquakes. *Nature*, 576(7785), 96–101. <https://doi.org/10.1038/s41586-019-1784-0>
- Satake, K., Fujii, Y., Harada, T., & Namegaya, Y. (2013). Time and space distribution of coseismic slip of the 2011 Tohoku earthquake as inferred from tsunami waveform data. *Bulletin of the Seismological Society of America*, 103(2B), 1473–1492. <https://doi.org/10.1785/0120120122>
- Scala, A. (2024). Dataset repository for paper “On the relation between seismic source dynamics, tsunami generation and propagation, and numerical modelling complexity for large earthquakes in subduction zones” [Dataset]. *Journal of Geophysical Research: Oceans*, Zenodo. <https://doi.org/10.5281/zenodo.10497580>
- Scala, A., Festa, G., & Vilotte, J.-P. (2017). Rupture dynamics along bimaterial interfaces: A parametric study of the shear-normal traction coupling. *Geophysical Journal International*, 209(1), 48–67. <https://doi.org/10.1093/gji/ggw489>
- Scala, A., Festa, G., Vilotte, J.-P., Lorito, S., & Romano, F. (2019). Wave interaction of reverse-fault rupture with free surface: Numerical analysis of the dynamic effects and fault opening induced by symmetry breaking. *Journal of Geophysical Research: Solid Earth*, 124(2), 1743–1758. <https://doi.org/10.1029/2018JB016512>
- Scala, A., Lorito, S., Romano, F., Murphy, S., Selva, J., Basili, R., et al. (2020). Effect of shallow slip amplification uncertainty on probabilistic tsunami hazard analysis in subduction zones: Use of long-term balanced stochastic slip models. *Pure and Applied Geophysics*, 177(3), 1497–1520. <https://doi.org/10.1007/s00024-019-02260-x>
- Selva, J., Lorito, S., Volpe, M., Romano, F., Tonini, R., Perfetti, P., et al. (2021). Probabilistic tsunami forecasting for early warning. *Nature Communications*, 12(1), 5677. <https://doi.org/10.1038/s41467-021-25815-w>
- Sepúlveda, I., Liu, P. L.-F., Grigoriu, M., & Pritchard, M. (2017). Tsunami hazard assessments with consideration of uncertain earthquake slip distribution and location. *Journal of Geophysical Research: Solid Earth*, 122(9), 7252–7271. <https://doi.org/10.1002/2017JB014430>
- Skarlatoudis, A. A., Somerville, P. G., & Thio, H. K. (2016). Source-scaling relations of interface subduction earthquakes for strong ground motion and tsunami simulation. *Bulletin of the Seismological Society of America*, 106(4), 1652–1662. <https://doi.org/10.1785/0120150320>
- Souty, V., & Gailler, A. (2021). Fast high-resolution S-PTHA along the Western Mediterranean sea coastlines. Application to the bay of Cannes. *Frontiers in Earth Science*, 9, 765610. <https://doi.org/10.3389/feart.2021.765610>
- Stefanakis, T., Dias, F., & Dutykh, D. (2012). Resonant long-wave run-up on A plane beach. In *Proceedings of the 22nd (2012) International offshore and Polar Engineering Conference* (pp. 116–121). Retrieved from <https://hal.science/hal-00728747>
- Stoker, J. J. (1992). *Water waves: The mathematical theory with applications*. Wiley Classic Library.

- Strasser, F. O., Arango, M. C., & Bommer, J. J. (2010). Scaling of the source dimensions of interface and Intraslab subduction-zone earthquakes with moment magnitude. *Seismological Research Letters*, 81(6), 941–950. <https://doi.org/10.1785/gssrl.81.6.941>
- Sugawara, D. (2021). Numerical modeling of tsunami: Advances and future challenges after the 2011 Tohoku earthquake and tsunami. *Earth-Science Reviews*, 214, 103498. <https://doi.org/10.1016/j.earscirev.2020.103498>
- Tadepalli, S., & Synolakis, C. E. (1994). The run-up of N-waves on sloping beaches. *Mathematical and Physical Sciences*, 445(1923), 99–112. <https://doi.org/10.1098/rspa.1994.0050>
- Takahashi, N., Kodaira, S., Tsuru, T., Park, J.-O., Kaneda, Y., Suyehiro, K., et al. (2004). Seismic structure and seismogenesis off Sanriku region, northeastern Japan. *Geophysical Journal International*, 159(1), 129–145. <https://doi.org/10.1111/j.1365-246X.2004.02350.x>
- Tanioka, Y., & Satake, K. (1996a). Fault parameters of the 1896 Sanriku tsunami earthquake estimated from tsunami numerical modeling. *Geophysical Research Letters*, 23(13), 1549–1552. <https://doi.org/10.1029/96GL01479>
- Tanioka, Y., & Satake, K. (1996b). Tsunami generation by horizontal displacement of ocean bottom. *Geophysical Research Letters*, 23(8), 861–864. <https://doi.org/10.1029/96GL00736>
- Tanioka, Y., & Seno, T. (2001). Sediment effect on tsunami generation of the 1896 Sanriku tsunami earthquake. *Geophysical Research Letters*, 28(17), 3389–3392. <https://doi.org/10.1029/2001GL013149>
- Thomas, M. Y., & Bhat, H. S. (2018). Dynamic evolution of off-fault medium during an earthquake: A micromechanics based model. *Geophysical Journal International*, 214(2), 1267–1280. <https://doi.org/10.1093/gji/ggy129>
- Tonini, R., Basili, R., Maesano, F. E., Tiberti, M. M., Lorito, S., Romano, F., et al. (2020). Importance of earthquake rupture geometry on tsunami modelling: The Calabrian arc subduction interface (Italy) case study. *Geophysical Journal International*, 223(3), 1805–1819. <https://doi.org/10.1093/gji/ggaa409>
- Uenishi, K., & Rice, J. R. (2003). Universal nucleation length for slip-weakening rupture instability under nonuniform fault loading. *Journal of Geophysical Research*, 108(B1). <https://doi.org/10.1029/2001JB001681>
- Ulrich, T., Gabriel, A. A., & Madden, E. H. (2022). Stress, rigidity and sediment strength control megathrust earthquake and tsunami dynamics. *Nature Geoscience*, 15(1), 67–73. <https://doi.org/10.1038/s41561-021-00863-5>
- Venkataraman, A., & Kanamori, H. (2004). Observational constraints on the fracture energy of subduction zone earthquakes. *Journal of Geophysical Research*, 109(B5). <https://doi.org/10.1029/2003JB002549>
- Wendt, J., Oglesby, D. D., & Geist, E. L. (2009). Tsunamis and splay fault dynamics. *Geophysical Research Letters*, 36(15). <https://doi.org/10.1029/2009GL038295>
- Wilson, A., & Ma, S. (2021). Wedge plasticity and fully coupled simulations of dynamic rupture and tsunami in the Cascadia subduction zone. *Journal of Geophysical Research: Solid Earth*, 126(7), e2020JB021627. <https://doi.org/10.1029/2020JB021627>
- Yamada, N., & Iwata, T. (2005). Long-period ground motion simulation in the Kinki area during the MJ 7.1 foreshock of the 2004 off the Kii peninsula earthquakes. *Earth Planets and Space*, 57(3), 197–202. <https://doi.org/10.1186/BF03351815>
- Ye, L., Lay, T., Kanamori, H., & Rivera, L. (2016). Rupture characteristics of major and great ($M \geq 7.0$) megathrust earthquakes from 1990 to 2015: I. Source parameter scaling relationships. *Journal of Geophysical Research: Solid Earth*, 121(2), 826–844. <https://doi.org/10.1002/2015JB012426>
- Yoshimoto, M., & Yamanaka, Y. (2014). Teleseismic inversion of the 2004 Sumatra-Andaman earthquake rupture process using complete Green's functions. *Earth Planets and Space*, 66(1), 152. <https://doi.org/10.1186/s40623-014-0152-4>

References From the Supporting Information

- Adsuara, J. E., Cordero-Carrión, I., Cerdá-Durán, P., & Aloy, M. A. (2016). Scheduled relaxation Jacobi method: Improvements and applications. *Journal of Computational Physics*, 321, 369–413. <https://doi.org/10.1016/j.jcp.2016.05.053>
- Beji, S., & Battjes, J. A. (1994). Numerical simulation of nonlinear wave propagation over a bar. *Coastal Engineering*, 23(1–2), 1–16. [https://doi.org/10.1016/0378-3839\(94\)90012-4](https://doi.org/10.1016/0378-3839(94)90012-4)
- Castro Díaz, M. J., & Fernández-Nieto, E. (2012). A class of computationally fast first order finite volume solvers: PVM methods. *SIAM Journal on Scientific Computing*, 34(4), A2173–A2196. <https://doi.org/10.1137/100795280>
- Chazel, F., Lannes, D., & Marche, F. (2011). Numerical simulation of strongly nonlinear and dispersive waves using a Green–Naghdi model. *Journal of Scientific Computing*, 48(1–3), 105–116. <https://doi.org/10.1007/s10915-010-9395-9>
- Chorin, A. J. (1968). Numerical solution of the Navier-Stokes equations. *Mathematics of Computation*, 22(104), 745. <https://doi.org/10.2307/2004575>
- Dingemans, M. W. (1994). Mast project I: Waves G8-M comparison of computations with Boussinesq-like models and laboratory measurements.
- Kazolea, M., & Delis, A. I. (2013). A well-balanced shock-capturing hybrid finite volume–finite difference numerical scheme for extended 1D Boussinesq models. *Applied Numerical Mathematics*, 67, 167–186. <https://doi.org/10.1016/j.apnum.2011.07.003>
- Ricchiuto, M., & Filippini, A. G. (2014). Upwind residual discretization of enhanced Boussinesq equations for wave propagation over complex bathymetries. *Journal of Computational Physics*, 271, 306–341. <https://doi.org/10.1016/j.jcp.2013.12.048>
- Titov, V. V., & Synolakis, C. E. (1995). Modeling of breaking and nonbreaking long-wave evolution and runup using VTCS-2. *Journal of Waterway, Port, Coastal, and Ocean Engineering*, 121(6), 308–316. [https://doi.org/10.1061/\(ASCE\)0733-950X\(1995\)121:6\(308\)](https://doi.org/10.1061/(ASCE)0733-950X(1995)121:6(308))